

Towards Accurate Variational Quantum Simulation of Hydrogen Molecule with Superconducting Qubits



Malay Singh

Supervisors : Msc R. Sagastizabal Prof. L. DiCarlo

Department of Applied Physics
Delft University of Technology

A thesis submitted in the partial fulfillment of the requirement for
the degree of Master in Applied Physics
To be defended publicly on 2nd July, 2018

Abstract

Malay Singh

Towards accurate quantum simulation of the hydrogen molecule using Superconducting Qubits

We implement a two-qubit variational quantum simulation to compute the ground state energy of the hydrogen Hamiltonian and study the error in it's estimate. The procedure to compute ground state energy employed in this work, called Variational Quantum Eigensolver(VQE) relies on the variational principle of quantum mechanics to find the ground state energy. Computing the ground state energy of the hydrogen molecule for the entire dissociation curve up to the benchmark of chemical accuracy on a quantum computer has remained an outstanding challenge. To address this challenge, we design and test through numerics two techniques which can improve the energy estimate and suppress the error below chemical accuracy. The first is called technique relies on the symmetry properties of the hydrogen Hamiltonian, to compensate for the effect of errors due to qubit relaxation(T_1), we show two different ways to do it. The second is called Active Error Mitigation(AEM), it relies on the dependence of error on the circuit length, which can be controlled by adding waiting gates. The error is suppressed through extrapolation of the energy estimate to the limit of zero circuit length.

We demonstrate through experiments on a superconducting quantum processor the implementation of the VQE algorithm. The error in the computed ground state energies are between 1 to 2 order of magnitude higher than chemical accuracy. Implementing the T_1 mitigation technique by rescaling suppresses the error by 1 order of magnitude. This work paves the way for accurate variational simulations of quantum chemistry problems on near-term quantum processors, which are expected to be noisy, hence require error mitigation techniques.

Acknowledgements

I would like to express my gratitude towards Prof. DiCarlo for giving me the opportunity to work in his lab and for continued guidance on this project. I have learned from you what it means to do good work and take data-driven decisions. DC lab has been an amazing place to work and I met many productive scientists who work tirelessly to build a quantum computer.

I would like to thank my direct supervisor Ramiro for his continued guidance and support. Your speed and can-do attitude has made my Masters Thesis a thrilling experience. We have come a long way in our project in the past 9 months, starting from only a vague idea of an experiment and no device to do it on, to a running experiment which has already produced novel insights into accurate quantum simulations. We have worked very closely on this experiment and I have had a lot to learn from you.

I would like to thank Lieven Vandersypen, Toeno Van Der Sar and Michael Wimmer for accepting my request to be in the thesis committee.

I would like to thank our collaborating theorists Thomas O'Brien and Xavier Bonet Monroig, for fruitful discussions. In particular I would like to thank Tom for conceiving the T₁ mitigation technique, co-developing the quantumsim software package and Xavi for numerical simulations of Quantum Subspace expansion. The quantumsim software package has been a great aid to understand the capabilities of our device and our error mitigation techniques. I thank Brian Tarasinski for co-developing it and helping me out several times when I ran into problems.

Furthermore, I would like to thank Niels Bultink for help with multiplexed readout and countless other experimental problems that we faced during setting up measurements with our awesome control electronics stack. DC lab has a great team of electronics engineers including but not limited to Jacob, Xiang, Jules, Greco and Wouter and their expertise in their respective fields has given us instruments which

run our small quantum processor. I thank Jacob de Sterke for providing us with his "reserved for research" CC-light, without it we would have not reached anywhere close to where we are now. Also, your adult supervision during assembling our rack was much appreciated. I would also like to thank Xiang Fu for co-inventing the CC-Light and for help with several issues that we came across. Jules, you have been really proactive in assembling QWG for us and I really admired your research on temperature stability of QWG outputs. Ale and Nandini, your help with device fabrication has helped us get a device in time and I thank you for that.

One of the great things about DC lab is the python based software stack we use to analyze our day to day results, I thank Adriaan and Chris for pioneering it. Adriaan and Livio's research on accurate two-qubit gates has been important for our experiment. Furthermore, we have greatly benefited from Florian's expertise on dilution refrigerators and all the things that go in it. It has been a pleasure working on masters thesis alongside several other talented masters students. Rene, Marc and Joep, I have thoroughly enjoyed our discussions about the progress of our masters theses.

I would like to thank my parents Dinesh and Sarita for being the guiding light in my life, without your support I would have definitely not taken the decision to leave India. I would also like to thank my sister Mishu for keeping me motivated and taking care of mom and dad while I was away. Last but not the least, I want to thank my girlfriend Neha, for being the warmth in my life.

Contents

List of Figures	iii
List of Tables	ix
1 Introduction and Outline	1
2 The Hydrogen Problem	3
2.1 Introduction	3
2.2 Hydrogen Hamiltonian	3
2.3 Variational Quantum Eigensolvers	9
3 Numerical simulations of VQE algorithm	11
3.1 Error Signalling	15
3.2 Active Error Mitigation	16
3.3 T ₁ mitigation by rescaling in post-processing	22
3.3.1 Limitations of the simulations	23
4 Device Characterization	25
4.1 Continuous-wave measurements	26
4.1.1 VNA Scans for resonators	26
4.1.2 Resonator Powersweep	27
4.1.3 Resonator DAC arches	28
4.1.4 Two Tone Spectroscopy	28
4.1.5 Tracked qubit spectroscopy	29
4.1.6 Avoided Crossing	30
4.2 Time Domain Measurements	30
4.2.1 Qubit relaxation: T1	30
4.2.2 Qubit dephasing: Ramsey	31
4.2.3 Fast frequency qubit dephasing : Echo	32

CONTENTS

4.3	Qubits Summary	34
5	Experimental Methods	35
5.1	Control Electronics Stack	35
5.2	Single-Qubit gates	37
5.3	Tomography	40
5.4	Two-Qubit gates	45
5.4.1	Theory of Two-Qubit Gates	45
5.4.2	Correction of Flux-Line Distortions	47
5.4.3	Cryogenic Distortions	49
5.4.4	Implementation of iSWAP Gate For VQE experiments	52
6	Results	57
6.1	Variational quantum simulation without error mitigation	57
6.2	T ₁ mitigation by rescaling	64
6.3	Conclusion	66
7	Outlook	67
	References	69

List of Figures

2.1	Pre-factors of Pauli terms occurring in the Hydrogen Hamiltonian and the dissociation curve. The dissociation curve(dashed line) is obtained through numerical diagonalization.	7
2.2	Results from diagonalization of the Hydrogen Hamiltonian on a classical computer. (a) Plot of Hydrogen Energy Spectrum in Bravyi-Kitaev mapping. The blue curve depicts the hydrogen dissociation curve. The minima of the dissociation curve occurs at $R = 0.75 \text{ \AA}$, consistent with the equilibrium bond length of Dihydrogen.(b) The concurrence needed in a prepared ground state as a function of Bond Length. The concurrence is obtained by taking the eigenvector corresponding to the lowest state in the computational basis, and then using the eqn 2.11. The increasing trend shows that ground-states at higher R have higher entanglement.	8
2.3	Error in the Hydrogen ground state energy computation when when the Hartree-Fock(HF) state $ 01\rangle$ is used as the solution for all bond lengths. HF states serves as a good approximation for small bond lengths. Red line represents chemical accuracy (1.6 milli Hartree).	8
2.4	Flowchart outline of Variational Quantum Eigensolvers with classical resources in orange and Quantum Resources in Blue. The set of new parameters is $\vec{\theta}$ and the prepared state is $\rho(\vec{\theta})$. The pauli terms to be measured are IZ, ZI, ZZ, XX and YY and the energy is calculated by weighing the pauli terms by $g_i(R)$. The steps are repeated until convergence for every bond length, R.	10
3.1	Quantum circuit for the six parameter circuit implementing the hardware oriented Ansatz.T ₀ and T ₁ are tomographic pre-rotations used to measure the state in different basis to obtain all the expectation values.	12

LIST OF FIGURES

3.2	a. Quantum circuit for the particle number conserving Ansatz. The Z-gate and the swap are parameterizable. Measurement waiting gate is not shown but added to the simulation. b. Plot of Converged Energies(Hartree) across Bond lengths.	14
3.3	Error in energy estimate obtained by using PCA circuit(a), red line represents chemical accuracy. Errors are computed form the exact solution.b. Plot of iSWAP angle of the converged states(dots) and the exact solution(continuous line) across interatomic distances.	14
3.4	Error signalling circuit used to obtain the expectation value of XX operator. The rotations $Y_{\pi/2}$ and $Y_{-\pi/2}$ occuring next to each other are not compiled for clarity. The C-NOT gate is applied with qubit q0 as control and qubit q1 as target. It is compiled with a C-Phase.	16
3.5	Error in energy estimate obtained after T_1 mitigation measurement.	16
3.6	Quantum circuit used in the AEM protocol. A waiting gate is inserted after every single and two-qubit gate operations. T_0 and T_1 represent tomographic pre-rotations.	18
3.7	Error in energy estimate as a function of waiting time (dots). The total circuit length is three times the waiting time. Continuos lines depict a least squares fit to a third-order polynomial.	19
3.8	Error in energy estimate after applying active error Minimization. Also shown for comparison is the Bare VQE error curve. The extrapolated error(orange) is approximately an order of magnitude lower.	20
3.9	Error in energy estimate obtained after applying Active error Minimization on top of T_1 mitigation measurement(green diamonds). Also shown for comparison is the Bare VQE error curve(blue), T_1 mitigation measurement (yellow) and AEM(orange).	20
4.1	Three Qubit Transmon quantum processor. Qubits A and D2 will be used in the experiments.	25
4.2	Three resonators coupled to the Data top, Data bottom and Ancilla qubits, at -60 dBm(on the source).	26
4.3	A powersweep of the resonator. $\omega = 7.7341$ GHz and $\omega = 7.7376$ GHz. The powershift is 3.5 MHz for this resonator.	27

LIST OF FIGURES

4.4 Resonator DAC arch for the resonator that responds the most to flux bias on qubit A.	28
4.5 Two tone spectroscopy of qubit A at zero flux bias.	29
4.6 Tracked spectroscopy of qubit A with FBL of A (D3 on the plot)	30
4.7 Avoided Crossing between $ ge\rangle$ and $ eg\rangle$ states	31
4.8 T_1 measurement with an exponential fit. The last 4 points are taken for calibration of probabilities.	32
4.9 Ramsey measurement with a decaying cosine fit, $T_2^* = 17.73\mu s$. This data was taken in a cooldown different to the one in which the VQE experiments were performed. For complete qubit spec table please refer to the last section of this chapter.	32
4.10 T_2^{echo} measurement, with a decaying exponential fit. The fit reported an echo time of 15.8. This data was taken in a cooldown different to the one in which the VQE experiments were performed. For complete qubit spec table please refer to the last section of this chapter.	33
 5.1 Control Electronics stack used in the VQE experiments. Dashed(continuous) lines represent digital(analogue) signals. Central Controller(orange) delivers codeword triggers to the QWG- microwave(used for single qubit rotations), QWG-flux(used for two qubit gates) and the UHFQC(used for measurement).	36
5.2 Fidelity of Single-Qubit gates. (a) Results of an ALLXY experiment after a tuneup. On the x-axis, lowercase represents $\frac{\pi}{2}$ rotations.(b) Results of a single-qubit Randomized Benchmarking experiment after a tuneup. We achieve a single qubit clifford gate fidelity of 99.73%. In this qubit, the fraction of error caused by qubit relaxation($1 - F_{CL}^{T_1}$) over total error($1 - F_{CL}$) is 35.77%.	38
5.3 Tomography sequence for cardinal states on two qubits. Single qubit rotations R_0 and R_1 are used to prepare all 36 cardinal states. Single qubit rotations T_0 and T_1 are tomographic pre-rotations.	41
5.4 Plot of measurement values(y-axis) of each channel after removal of offsets and scaling for the state $ 01\rangle$, which in our convention is $ q_1q_0\rangle$. The sequence consists of 36 pre-rotations[ref (26)] followed by 7×4 calibration measurements(x-axis). Panel (a) qubit shows processed measurement results for q_0 , which is in the excited state. (b) qubit q_1 is in the ground state and (c) correlation of q_0 and q_1	42

LIST OF FIGURES

5.5	Pauli label plot and density matrix histogram of $ 01\rangle$	43
5.6	Energy level for virtual photon swap interaction. When both the qubits are detuned from the cavity(dashed black line), both the qubits dispersively shift the cavity. The excited state on the left qubit $ 1,0\rangle, n = 0$ interacts with the excited state on the right qubit $ 0,1\rangle, n = 0$ by the exchange of a virtual photon $ 0,0\rangle, n = 1$ in the cavity. In this diagram $\Delta_1 = \Delta_2 = \Delta$, corresponding to the resonance condition. Adapted from J.M. chow's thesis[ref (4)].	46
5.7	Orange curve depicts the measured output signal which has passed through all the room temperature components, for a square pulse input. Blue curve depicts the resulting signal after pre-distorting the square pulse using several models(see table). The deviation from the targetted square pulse was around 2%. The room temperature flux corrections are applied in the timescale of a typical experimental run, which in our case is 200	48
5.8	Amplitude calibration arc (a) obtained through a cryoscope experiment repeated for different flux pulse amplitudes. The detuning of the qubit increases with increasing amplitude. Distortions in flux pulses lead to a smearing of peaks. The right panel shows instantaneous detuning as a function of flux pulse length for an amplitude of 700 mV, which will be used to bring the qubit being fluxed(A) into an avoided crossing with the other qubit (D2). Data in (b) was obtained after correcting for bounces, therfore corresponds to Fig 5.9 (b). The detuning reported here is 500 MHz(QWG samples at 1ns) less than the actual detuning because we are at the second Nyquist order.	49
5.9	Cryogenic step response measured using a cryoscope before (a) and after applying two bounce corrections at 15ns and 8ns with amplitudes	50
5.10	Measurement of coherent oscillations(the chevron pattern) at the $ 01\rangle \leftrightarrow 10\rangle$ avoided crossing after correcting for distortions. The central slice of the chevron represents the amplitude(of the flux pulse) at which qubit A comes into resonance with qubit D2 and hence the iSWAP gate is implemented as a vertical cut of this plot. The oscillations along y-axis represent exchange in populations between the two qubits.	51

LIST OF FIGURES

5.11	Expectation Values of Pauli operators $\{IZ, ZI, ZZ, XX, XY, YX, YY\}$ as a function of flux pulse length. The operator sets $\{XX, XY\}$ (orange dots) and $\{YY, YX\}$ (red dots) are clubbed together to correct for the phase acquired by the qubit being fluxed. Grey vertical lines denote the \sqrt{iSWAP} point, where maximum concurrence is reached in the prepared state. Magenta vertical line represents the iSWAP point, where the population exchange is completed(red and green dots).	53
5.12	Phase acquired by the qubit being fluxed(A). The rapid oscillations are due to the large detuning A from it's sweetspot. The oscillations start at 3ns, corresponding to the rise time of the flux pulse and experience a 180 degree jump at 15 ns(iSWAP point).	54
5.13	Top panel shows phase acquired by the qubit not being fluxed(D2) as a function of flux-pulse length. Also shown below is the excitation probability of the same qubit. Since the qubit starts in the state $ -i \rangle$, the excitation probability $\langle Z \rangle = \frac{1}{2}$. After completely exchanging the population(at the iSWAP point), the state of the qubit is $ 0 \rangle$. At the iSWAP point we get a 180 degree phase jump, because the coherence term acquires a factor of -1.	54
5.14	Pauli label plot(left) and denisty matrix histogram(right) of the Bell-State $ \Psi^+\rangle = \frac{ 01\rangle + 10\rangle}{\sqrt{2}}$ obtained through Least-Squares Tomography. The reported fidelity is obtained by contracting a vector of all pauli terms with a vector of pauli labels for the ideal Bell state. A maximum likelihood tomography of the same data gave a fidelity of 94.8%	56
6.1	Expectatation values of Pauli terms as a function of θ (angle of iSWAP) and ϕ (phase correction gate). (a) $\langle IZ \rangle$, (b) $\langle ZI \rangle$, (c) $\langle ZZ \rangle$ and (d) $\langle XX \rangle$. In the phase convention of this plot singlet bell states are formed at $\phi = 0$ and 2π	58
6.2	Energy landscapes obtained after mapping the expectation values obtained through tomography in (a), (c) and (d). Energy landscapes obtained through a quantum-sim simulation of the same circuit in (b), (d) and (e). The simulated landscapes have a much smaller discretization. The minima of the landscapes are shown as red stars. For the simulation data all minimas lie on the segment $\phi = 0$, but for the experimental data they all lie on the axis $\phi = 2\pi$. The simulations are periodic, with a period of 2π along y-axis.	60

LIST OF FIGURES

6.3 Results from a VQE experiment. (a) Plot of experimentally computed ground state energy (dark blue). Also shown are ground state energies obtained via numerical diagonalization (light blue) and simulation with a basic error model.(b) Plot of the error in the energy estimation.	61
6.4 Experimentally obtained expectation values of pauli terms(filled circles) occurring in the hydrogen Hamiltonian of eqn 2.10. Also shown are expectation values calculated via numerical diagonalization(continuous lines) and via coherence limited simulation(empty circles).	62
6.5 Control parameters as function of bond length. Angle of iSWAP in (a) as a function of bond length obtained from experiment (blue filled circles). There are only 8 unique values of theta as the flux pulse takes the values from $t = 0$ ns to 7 ns in steps of 1 ns. The disagreement between experimental data and simulation/theory is likely due to a low pass effect which results in qubits to not exchange any populations between states $ 01\rangle$ and $ 10\rangle$ when the flux pulse is small. For comparison theory and simulation results with two different offsets with 1.6 ns and 2.6 ns are also shown. The values for predicted ϕ are in well agreement with the theory as both values 0 and 2π produce the same energy in theory.	62
6.6 Results from a VQE experiment with T_1 mitigation. (a) Plot of expectation values as a function of bond length for three sets of data; experiment, theory and simulation. The parity, $\langle ZZ \rangle$ is equal to -1 for theory, experiment and simulation. $\langle XX \rangle = \langle YY \rangle$ are equal for all three sets of data. This signals a successful enforcement of parity conservation.	64
6.7 Error in Energy estimate. T_1 mitigation results in one to two orders of magnitude in error reduction. After error mitigation we see an increasing trend in error this is because we still have errors caused by finite T_2 , these become more prominent as concurrence becomes higher.	65

List of Tables

2.1	The five classes of hermitian second quantized operators that appear in electronic hamiltonians. The one and two electron overlap integrals h_{ij} and h_{ijkl} depend on bond length.	5
5.1	Table of β s, in the order channel q_0 , channel q_0 , channel correlation(q_0, q_1) from top to bottom.	41
5.2	Summary of fit parameters for Room Temperature corrections.	48

LIST OF TABLES

1

Introduction and Outline

One of the proposed powerful applications for near-term quantum computers is to address problems in quantum simulation of molecular structures and condensed matter physics problems, which currently stretch the limits of existing high-performance computing infrastructure[ref (20)]. In the near term quantum devices will lack the resources for full fault tolerance and therefore will be significantly error prone. Algorithms on Hybrid quantum-classical systems such as Variational Quantum Eigensolvers[ref (9)] have been implemented to solve for the ground state energy of a molecular Hamiltonian mapped onto a system of Qubits. They require shallow circuits for variational state preparation whose output is fed into a classical supervising algorithm. The use of many iterations of shallow circuits helps achieve lower error rates in energy estimate as compared to quantum phase estimation algorithm[ref (22)]. In this project we aim to experimentally study error mitigation strategies which enhance the accuracy of energy estimate. In the **second chapter** we give a brief explanation of the hydrogen hamiltonian and show the procedure to map it onto qubits. We also report results from numerical diagonalization of the hydrohen Hamiltonian and the property of it's ground states. In the **third chapter** we study numerical simulation of the VQE algorithm and design techniques to mitigate it. We support our claims with simulations in which the quantum state preparation part is done using the quantumsim[ref (38)] simulator developed in the DiCarlo lab by Brian Tarasinski and T.E. O'Brien.

In the **fourth chapter** we report the characterization of a Three Qubit device which will be used to implement these protocols. We use the characterized parameters of the device throughout our simulations. In the **fifth chapter** we report the developement of experimental methods necessary to execute the VQE algorithm on the characterized quantum processor. In particular we develop the two-qubit iSWAP(θ) gate necessary for the implementation of VQE

1. INTRODUCTION AND OUTLINE

algorithm described in chapter three. In the **sixth chapter** we report the results of an ongoing experiment. We implement the VQE algorithm and study the errors obtained in the energy estimate. We then move on to implementing an error mitigation technique which suppresses the errors caused by qubit relaxation.

2

The Hydrogen Problem

2.1 Introduction

One of the central problems in quantum chemistry is to compute the ground state energy of the molecular electronic structure Hamiltonian. The accuracy of this result is commonly benchmarked by the standard of chemical accuracy. Chemical energy is an important benchmark for this particular problem, other problems in quantum chemistry require different benchmarks, for example spectroscopic accuracy. The value of chemical accuracy in computational chemistry comes from the desire to match or exceed experimental accuracy in thermochemical experiments which are accurate upto 1 kcal per mole[ref (40)]. Converting to atomic units of energy(defined in the section 2.2) by using a conversion factor 1 Hartree= $4.35974417(75) \times 10^{-18}$ J, the chemical accuracy is 1.6 milli Hartree in the atomic units of energy. Chemical accuracy corresponds to .1 percent error in energy estimation, for the case of hydrogen molecule, but in general depends on the energy scales of molecules. Reaching this goal for the entire dissociation curve for the smallest molecule, Hydrogen (H_2) has proven to be difficult with quantum simulations using state-of-the art superconducting qubits[ref (21)]. In the next section we briefly discuss the procedure to map molecular electronic stucture Hamiltonian of H_2 on to qubits. Then we elucidate important properties of the Hydrogen Hamiltonian and it's ground state. In the last section, we lay down the theory of variational quantum simulations[ref (17)].

2.2 Hydrogen Hamiltonian

The molecular electronic structure Hamiltonian describes the interaction between electrons and nuclei in a Coulomb potential[ref (45)]. Consider a collection of nuclear charges Z_i with N number of electrons in the system. The position of i th electron is r_i and R_i, M_i, Z_i are the

2. THE HYDROGEN PROBLEM

position, mass and charge of the nuclei respectively. The dynamics of this system is represented by molecular structure Hamiltonian in the first quantization

$$\mathcal{H} = - \sum_i \frac{\nabla_{R_i}^2}{2M_i} - \sum_i \frac{\nabla_{r_i}^2}{2} - \sum_{i,j} \frac{Z_i}{|R_i - r_j|} + \sum_{i,j>i} \frac{Z_i Z_j}{|R_i - R_j|} + \sum_{i,j>i} \frac{1}{|r_i - r_j|}. \quad (2.1)$$

Here the energy units is the atomic unit of energy, Hartree defined as

$$1 \text{ Hartree} = \frac{\hbar^2}{m_e e^2 a_0^2} \quad (2.2)$$

Where m_e, e, a_0 denote the mass of electron, charge of electron and Bohr radius respectively. The Hamiltonian of eqn 2.1 is of central importance in quantum chemistry as it's eigenstates determine the dynamics of the molecule. For example, a chemical reaction occurs when the system evolves from one stable chemical structure to another. The energy difference between two stable configurations along with ambient conditions determine the rate of chemical reactions. Therefore, accurate calculation of ground and a few excited states are necessary to understand complex chemical reactions. Previous works have directly mapped eq to qubits[ref (15)], however in this work we first express this hamiltonian in second quantization. We follow the prescription given by Whitfield et al as given in [ref (32)]. The first step is to approximate the nuclei as fixed classical point charges by invoking the Born-Oppenheimer approximation. The approximation works because mass of nuclei is at least three orders of magnitude larger than electron mass, hence the nuclear motion is much slower. Therefore, nuclei can be treated as fixed classical point charge. Next, a basis to represent the wave-function of the electrons $\phi_i(r_i, s_i)$ is chosen. Here r_i and s_i are the position and spin coordinate respectively. The position and momentum of electron are then expressed in terms of creation and annihilation operators a_i^\dagger, a_j which obey the fermionic anti-commutation relations

$$\{a_i, a_j^\dagger\} = \delta_{i,j}, \{a_j, a_i^\dagger\} = 0. \quad (2.3)$$

The second quantized Hamiltonian is given by

$$\hat{\mathcal{H}} = \sum_{p,q} h_{pq} a_p^\dagger a_q + \sum_{p,q,r,s} h_{pqrs} a_p^\dagger a_q^\dagger a_r a_s \quad (2.4)$$

$$= \hat{\mathcal{H}}^{(1)} + \hat{\mathcal{H}}^{(2)}. \quad (2.5)$$

Where the coefficents h_{pq} and h_{pqrs} are calculated from:

$$h_{pq} = \int d\sigma \phi_p^*(\sigma) \left(\frac{\nabla_r^2}{2} - \sum_i \frac{Z_i}{|R_i - r|} \right) \phi_q(\sigma) \quad (2.6)$$

$$h_{pqrs} = \int \int d\sigma_1 d\sigma_2 \frac{\phi_p^*(\sigma_1) \phi_q^*(\sigma_2) \phi_s(\sigma_1) \phi_r(\sigma_2)}{|r_1 - r_2|}. \quad (2.7)$$

Where p, q refers to the fermionic modes, the creation and annihilation operators on them obey fermionic commutation rules. The basis functions $\{\phi_i(\sigma_i)\}$ form a minimal basis set. A minimal basis set is where only sufficient orbitals are used to contain all the electrons in the neutral atom. The minimal basis set contains sufficient orbitals to cover the highest-occupied shell of the free atom (e.g. for H2, we take both 1s orbitals). h_{pq} and h_{pqrs} are one-body and two-body integrals over new spacial and spin coordinates with $\sigma_i = (r_i, s_i)$. They depend on bond length R . The one-electron Hamiltonian

$$\mathcal{H}^{(1)} = h_{11}a_1^\dagger a_1 + h_{22}a_2^\dagger a_2 + h_{33}a_3^\dagger a_3 + h_{44}a_4^\dagger a_4,$$

and the two-electron Hamiltonian

$$\begin{aligned} \mathcal{H}^{(2)} = & h_{1221}a_1^\dagger a_2^\dagger a_2 a_1 + h_{3443}a_3^\dagger a_4^\dagger a_4 a_3 + h_{1441}a_1^\dagger a_4^\dagger a_4 a_1 \\ & h_{2332}a_2^\dagger a_3^\dagger a_3 a_2 + (h_{1331} - h_{1313})a_1^\dagger a_3^\dagger a_3 a_1 + (h_{2442} - h_{2424})a_2^\dagger a_4^\dagger a_4 a_2 + \\ & h_{1423}(a_1^\dagger a_4^\dagger a_2 a_3 + a_3^\dagger a_2^\dagger a_4 a_1) + h_{1243}(a_1^\dagger a_2^\dagger a_4 a_3 + a_3^\dagger a_2^\dagger a_4 a_1) + \\ & h_{1423}(a_1^\dagger a_4^\dagger a_2 a_3 - a_3^\dagger a_2^\dagger a_4 a_1) + h_{1234}(a_1^\dagger a_2^\dagger a_4 a_3 - a_3^\dagger a_2^\dagger a_4 a_1), \end{aligned}$$

contain 5 classes of fermionic operators summarized in the table below[ref (31)]. This second

Operator	Second quantized form
Number Operator	$h_{ii}a_i^\dagger a_i$
Coulomb/exchange operators	$h_{ijji}a_i^\dagger a_j^\dagger a_j a_i$
Excitation operator	$h_{ij}(a_i^\dagger a_j + a_j^\dagger a_i)$
Number excitation operator	$h_{ijjk}(a_i^\dagger a_j^\dagger a_j a_k + a_k^\dagger a_j^\dagger a_j a_i)$
Double excitation operator	$h_{ijkl}(a_i^\dagger a_j^\dagger a_k a_l + a_l^\dagger a_k^\dagger a_j a_i)$

Table 2.1: The five classes of hermitian second quantized operators that appear in electronic hamiltonians. The one and two electron overlap integrals h_{ij} and h_{ijkl} depend on bond length.

quantized Hamiltonian must now be mapped onto a system of qubits, to this end we need to express the second quantized Hamiltonian in terms of Pauli operators. The two most common mappings in the literature are the Bravyi-Kitaev and the Jordan-Wigner mapping. The Jordan-Wigner transform represents the occupation of each orbital with the state of a single-qubit,

2. THE HYDROGEN PROBLEM

this is called the occupation basis[ref (39)]. Consider a state with n orbitals where f_i is the occupation of orbital i , $|f_{n-1}...f_0\rangle$, when applying the creation operator a_j^\dagger , the state acquires a phase of -1 for each occupied orbital with index less than j ; that is

$$a_j^\dagger |f_{n-1}...f_{j+1}, 0, f_{j-1}...f_0\rangle = (-1)^{\sum_{k=0}^{j-1} f_k} |f_{n-1}, ..., f_{j+1}, 1, f_{j-1}...f_0\rangle \quad (2.8)$$

This implies that the qubit implementation of the operator a_j^\dagger must contain not only a gate to change the value of qubit j but also must compute the parity of all qubits with index less than j ; the parity of all preceding qubits is evaluated using a Z operator on each. Therefore, one fermionic operation requires $O(n)$ gates, where n is the number of qubits[ref (36)]. Moreover, these gates are non-local. Another possible encoding is the parity basis, where qubit j now stores the parity of all orbitals with index less than or equal to j . In this case, when applying a_j^\dagger the phase acquired due to the parity of all orbitals with index less than j is computed with a Z gate on qubit $j - 1$. However, we loose the advantage generated by this encoding when changing the occupation of orbital j , all qubits with index $\geq j$ must be updated. Therefore one fermionic operation requires $O(n)$ gates again. In their seminal publication[ref (42)], S.B. Bravyi and A.Yu. Kitaev develop a middle-ground mapping in which both occupation and parity are stored non-locally instead of occupation locally and parity non-locally like in occupation basis (and vice-versa for parity basis). For even index j , qubit j holds the occupation of orbital j . For odd j , qubit j stores the parity of a set of orbitals with index less than j . This results in an $O(\log(n))$ number of gates to simulate one fermionic operator. The Bravyi-Kitaev(BK) transformation is defined by an n -by- n matrix β_n , where $\beta_n \vec{f}_n = \vec{b}_n$ with the occupation number basis vector \vec{f}_n and the BK basis \vec{b}_n [ref (39)]:

$$\beta_{2^x} = \left[\begin{array}{c|c} \beta_{2^{x-1}} & 0 \\ \hline 0 & \beta_{2^{x-1}} \\ \leftarrow ...1... \rightarrow & \end{array} \right]$$

where $\leftarrow ...1... \rightarrow$ represents a row of ones.

Computing the mapping of all the operators occurring in the Hamiltonian is beyond the scope of this thesis. For a complete calculation look at [ref (31)]. The Bravyi-Kitaev transformation[ref (42)], results in the following form[ref (22)]:

$$\begin{aligned} \hat{\mathcal{H}} = & f_0 \mathbb{1} + f_1 Z_0 + f_2 Z_1 + f_3 Z_2 + f_1 Z_0 Z_1 \\ & + f_4 Z_0 Z_2 + f_5 Z_1 Z_3 + f_6 \textcolor{blue}{X_0} Z_1 \textcolor{blue}{X_2} + f_6 \textcolor{blue}{Y_0} Z_1 \textcolor{blue}{Y_2} \\ & + f_7 Z_0 Z_1 Z_2 + f_4 Z_0 Z_2 Z_3 + f_3 Z_1 Z_2 Z_3 \\ & + f_6 \textcolor{blue}{X_0} Z_1 \textcolor{blue}{X_2} Z_3 + f_6 \textcolor{blue}{Y_0} Z_1 \textcolor{blue}{Y_2} Z_3 + f_6 Z_0 Z_1 Z_2 Z_3. \end{aligned} \quad (2.9)$$

2.2 Hydrogen Hamiltonian

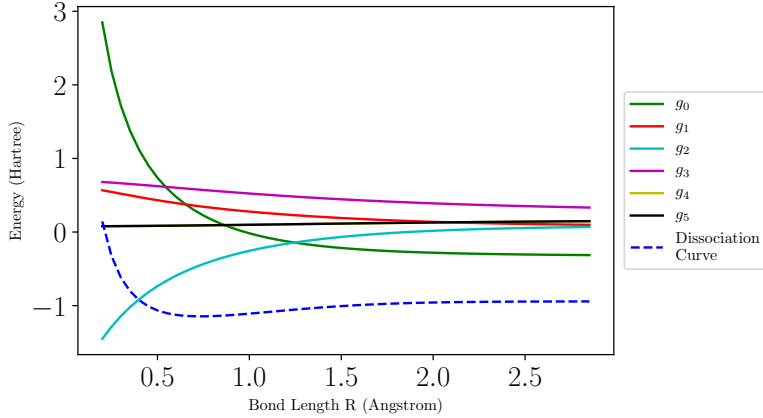


Figure 2.1: Pre-factors of Pauli terms occurring in the Hydrogen Hamiltonian and the dissociation curve. The dissociation curve(dashed line) is obtained through numerical diagonalization.

Where $\{f_i\}$ depends on the bond length of H_2 molecule. This Hamiltonian acts off-diagonally on only two qubits, the ones having tensor labels 0 and 2 (blue).

$$[\hat{\mathcal{H}}, Z_1] = [\hat{\mathcal{H}}, Z_3] = 0$$

The qubits with tensor labels 1 and 3 are never flipped during the simulation. We can use this symmetry to scalably reduce the Hamiltonian of eqn 2.9 down to two qubits. Here $\mathbb{1}$, X_i , Y_i and Z_i are Pauli operators acting on the i-th qubit. The Hamiltonian contains tensor products of operators e.g. $Z_0Z_1Z_2 = Z_0 \otimes Z_1 \otimes Z_2 \otimes \mathbb{1}_3$. After removing the qubits corresponding to the tensor labels 1 and 3, the hamiltonian is given by[ref (22)]

$$\hat{\mathcal{H}}_{2Q} = g_0(R)\mathbb{1} + g_1(R)IZ + g_2(R)ZI + g_3(R)ZZ + g_4(R)XX + g_5(R)YY. \quad (2.10)$$

The prefactors $\{g_i\}$ of pauli terms occurring in this hamiltonian are inherited from the overlap integrals given by eqns 2.6 and 2.7. They depend on the bond length R. One could use the software package OpenFermion[ref (18)] and Psi4[ref (44)] to these calculations, however in our work so far we have used the prefactors published in the work of O'Malley et. al[ref (22)]. The pre-factors g_4 and g_5 of operators XX and YY are equal and take values .07 to .14 Hartree. These prefactors govern the amount of entanglement required in the ground state. The increasing trend with respect to R means that ground states prepared on the quantum computer will require an increasing amount of entanglement as R increases. The pre-factor of ZZ , g_3 is always positive. The Hydrogen Hamiltonian $\hat{\mathcal{H}}_{2Q}$ commutes with the parity operator ZZ ,

2. THE HYDROGEN PROBLEM

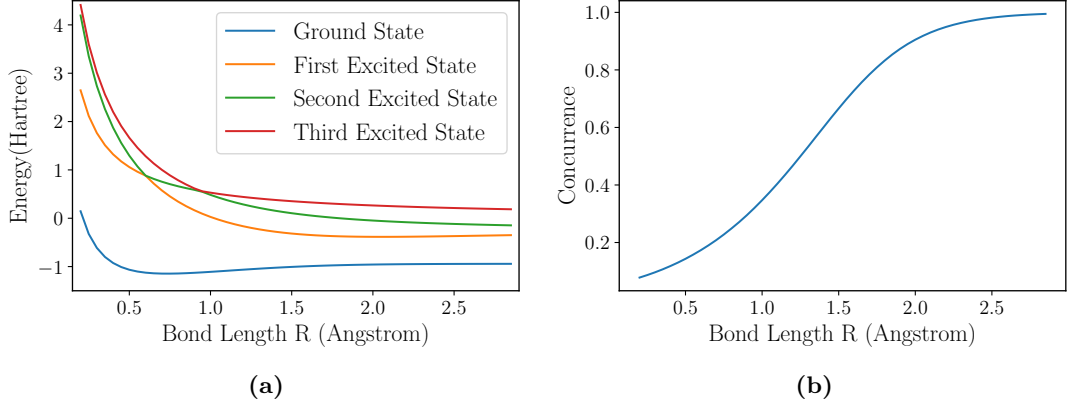


Figure 2.2: Results from diagonalization of the Hydrogen Hamiltonian on a classical computer. (a) Plot of Hydrogen Energy Spectrum in Bravyi-Kitaev mapping. The blue curve depicts the hydrogen dissociation curve. The minima of the dissociation curve occurs at $R = 0.75 \text{ \AA}$, consistent with the equilibrium bond length of Dihydrogen.(b) The concurrence needed in a prepared ground state as a function of Bond Length. The concurrence is obtained by taking the eigenvector corresponding to the lowest state in the computational basis, and then using the eqn 2.11. The increasing trend shows that ground-states at higher R have higher entanglement.

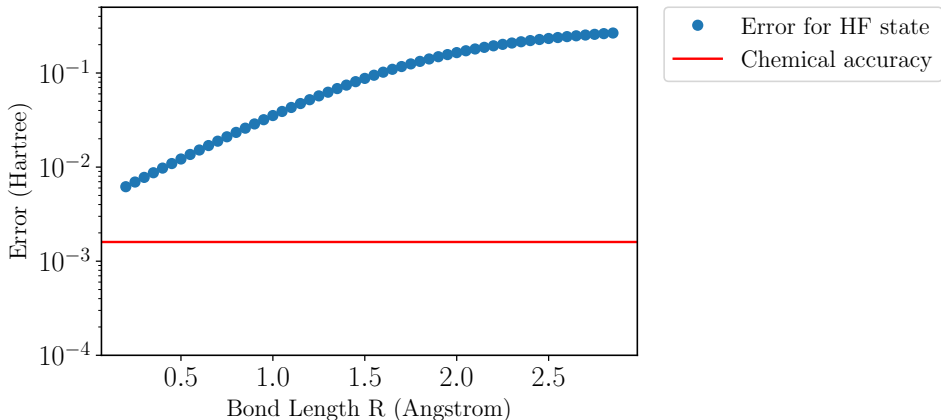


Figure 2.3: Error in the Hydrogen ground state energy computation when the Hartree-Fock(HF) state $|01\rangle$ is used as the solution for all bond lengths. HF states serves as a good approximation for small bond lengths. Red line represents chemical accuracy (1.6 milli Hartree).

$$[\hat{\mathcal{H}}_{2Q}, ZZ] = 0, \quad (2.11)$$

this implies that the eigenstates of the Hamiltonian have a definite parity. Furthermore, $|01\rangle$ is the Hartree-Fock (mean field) state of molecular hydrogen in the representation of eq. 2.10. The HF state has a non-trivial overlap with true ground state of molecular hydrogen, therefore we can conclude that the parity of true ground state is odd[ref (22)]. The odd parity subspace is spanned by the basis vectors $\{|01\rangle, |10\rangle\}$. The general solution to the hydrogen ground state is

2.3 Variational Quantum Eigensolvers

given by $\cos(\theta) |01\rangle - \sin(\theta) |10\rangle$, where θ depends on R. We will use the ZZ symmetry property to design efficient circuits and error mitigation techniques(Ch3). We diagonalize the Hamiltonian of eq 2.10 and plot the energy spectrum in fig 2.2(a). We also plot the concurrence(C) of the ground state as a function of bond length in fig 2.2(b). The concurrence C expressed in terms of computational basis coefficients, is given by

$$C = 2 |\alpha_{00}\alpha_{11} - \alpha_{01}\alpha_{10}| . \quad (2.12)$$

The increasing trend of this curve shows that ground states at high bond length need higher entanglement.

Before we move onto quantum simulations of molecular hydrogen, we evaluate the error in ground state energy estimation if Hartree-Fock(mean field) approximation to the hydrogen ground state is used as the ground state for all bond lengths. The error as a function of bond length shows that HF serves as a good approximation only for small bond lengths. This is consistent with the observation that at high bond lengths entanglement is a key requirement.

2.3 Variational Quantum Eigensolvers

The Variational Quantum Eigensolver(VQE) is a hybrid quantum-classical algorithm that uses low depth quantum circuits at the expense of increased number of iterations to converge to the ground state of a problem Hamiltonian. It was introduced by Peruzzo et.al(9) in the context of Photonics. It involves preparing a parameterized wavefunction $|\psi(\vec{\theta})\rangle$ and then estimating the energy $\langle\psi(\vec{\theta})| \hat{H} |\psi(\vec{\theta})\rangle$, and minimizing this energy. The variational principle states that for all $\{\vec{\theta}\}$:

$$\frac{\langle\psi(\vec{\theta})| \hat{H} |\psi(\vec{\theta})\rangle}{\langle\psi(\vec{\theta})| \psi(\vec{\theta})\rangle} \geq E_{GS} \quad (2.13)$$

This means that the ground state energy is the minima of the measured energy landscape. The basic algorithm is as follows:

- **Encode** the real space molecular Hamiltonian onto qubits.
- **Use a parameterized ansatz** capable of representing the ground state of the problem Hamiltonian. An ansatz is a set of parameterized wavefunctions that can approximate a parameter.

2. THE HYDROGEN PROBLEM

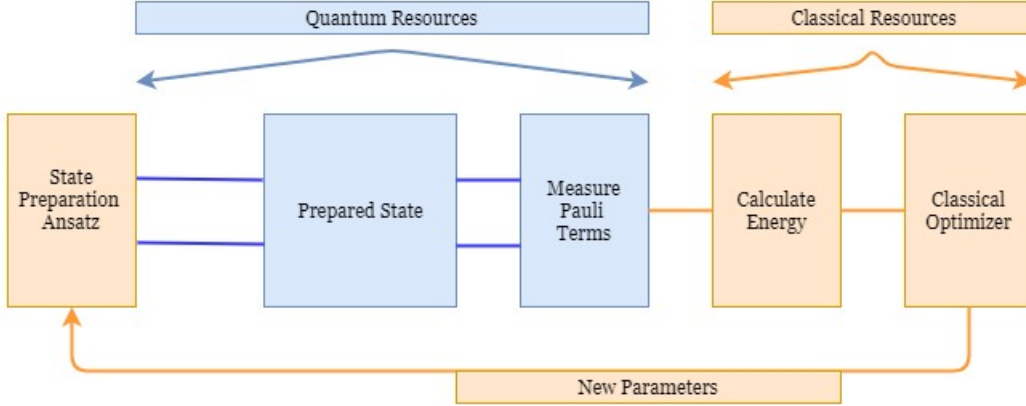


Figure 2.4: Flowchart outline of Variational Quantum Eigensolvers with classical resources in orange and Quantum Resources in Blue. The set of new parameters is $\vec{\theta}$ and the prepared state is $\rho(\vec{\theta})$. The pauli terms to be measured are IZ, ZI, ZZ, XX and YY and the energy is calculated by weighing the pauli terms by $g_i(R)$. The steps are repeated until convergence for every bond length, R.

- **Measure each Pauli term** in the Hamiltonian and classically compute the energy by weighing the pauli terms according to mapping generated in step 1. The computed energy is a function of parameters $\vec{\theta}$ and serves as a cost function.
- **Feed the cost function** into a (classical) minimization routine to generate new set of parameters. Repeat until a convergence criterion is met.

The choice of Ansatz is crucial to success and scalability of VQE. Using a classical minimization routine to search the solution space gives the VQE a hybrid quantum-classical character[ref (21)]. In the next chapter we explore two ansatze a hardware oriented ansatz(HOA) and a particle number conserving ansatz (PCA). PCA reduces the number of parameters by employing the knowledge of subspace in which the solution of the ground state of Hydrogen Hamiltonian lies. We build a robust error mitigation techniques on top of this.

3

Numerical simulations of VQE algorithm

This chapter deals with the design of quantum circuits that will be used to prepare parameterized quantum states which will encode the ground state of the Hydrogen Hamiltonian. The set of parameterized states are called Ansatz. In previous works different strategies like Unitary Coupled Cluster Ansatz(UCC)[ref (22)] and Hardware oriented Ansatz[ref (8)] have been implemented. We first give an overview of Hardware oriented Ansatz. We then move on to Particle Number Conserving Ansatz(PCA), which we study through numerical simulations in quantumsim. The idea of HOA is to develop a circuit that can be used to prepare any two-qubit pure state. Since any two-qubit pure state can be described by 6 real parameters this circuit uses six parameters to parameterize the trial wave function. To design this circuit we use two single qubit rotations with two parameters each. An arbitrary single qubit rotation is defined as [ref (5)]:

$$U_{\theta,\phi,\lambda} = \begin{bmatrix} \cos(\frac{\theta}{2}) & -i \exp(i\lambda) \sin(\frac{\theta}{2}) \\ -i \exp(i\phi) \sin(\frac{\theta}{2}) & \exp(i(\lambda + \phi)) \cos(\frac{\theta}{2}) \end{bmatrix} \quad (3.1)$$

We can compile any arbitrary single qubit rotation as (10):

$$U_{\theta,\phi,\lambda} = R_{\hat{Z}}(\phi)R_{\hat{X}}(\theta)R_{\hat{Z}}(\lambda) \quad (3.2)$$

Here $R_{\hat{Z}}(\phi)$, $R_{\hat{X}}(\theta)$ and $R_{\hat{Z}}(\lambda)$ are rotations about z-axis, x-axis and z-axis respectively. In our circuit we design single qubit gates which have two arbitrary parameters, this gate is obtained by setting $\phi = -\lambda$. To create necessary entanglement we use a parameterized iSWAP

3. NUMERICAL SIMULATIONS OF VQE ALGORITHM

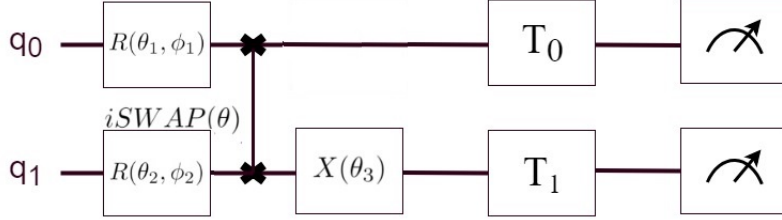


Figure 3.1: Quantum circuit for the six parameter circuit implementing the hardware oriented Ansatz. T_0 and T_1 are tomographic pre-rotations used to measure the state in different basis to obtain all the expectation values.

gate with the matrix representation given below[ref (23),(4)]:

$$U_{iSWAP}(\theta) = \begin{bmatrix} 1 & 0 & 0 & 0 \\ 0 & \cos(\theta) & -i\sin(\theta) & 0 \\ 0 & -i\sin(\theta) & \cos(\theta) & 0 \\ 0 & 0 & 0 & 1 \end{bmatrix} \quad (3.3)$$

Fig 3.1 shows the plot of this circuit, the first layer of single qubit gates uses a total of 4 parameters, next the $iSWAP(\theta)$ gate uses one parameter, the final single qubit gate is an X rotation i.e. $U(\theta, 0, 0)$. This circuit can prepare ground states of the hydrogen hamiltonian, but is inefficient in the number of parameters. Moreover it does not employ the knowledge of the ZZ symmetry of hydrogen Hamiltonian. As was explained in the last chapter, the solutions to the ground state lie in the odd parity subspace, i.e. $\langle ZZ \rangle = -1$. Therefore know that we need to put only one excitation in the prepared state i.e. start with a state $|01\rangle$. The first layer of single qubit gates can potentially add two excitations, whereas we only need one. This leads us to particle number conserving ansatz (PNC), which employs the knowledge of the symmetry of the hydrogen Hamiltonian. Here particle number is one, because we need to put only one excitation. It uses only 2 parameters, which are sufficient to parameterize any two-qubit pure state lying in the odd-parity subspace. This circuit enables the usage of T_1 error signalling technique introduced in the next section. In figure 3.2 (a) we propose a circuit which prepares an ansatz of the form

$\cos(\theta)|01\rangle - i\sin(\theta)\exp(i\phi)|10\rangle$ using a parameterizable $iSWAP(\theta)$ gate, as introduced in equation 3.3. The concurrence C of any two-qubit pure state $|\psi\rangle_{2Q}$ is defined as

$$|\psi\rangle_{2Q} = \alpha_{00}|00\rangle + \alpha_{01}|01\rangle + \alpha_{10}|10\rangle + \alpha_{11}|11\rangle \quad (3.4)$$

$$C = 2 |\alpha_{00}\alpha_{11} - \alpha_{01}\alpha_{10}|. \quad (3.5)$$

C for PNC goes as $\sin(2\theta)$, therefore we prepare states of higher entanglement as the angle of the iSWAP(θ) increases. To simulate this circuit we use the quantumsim density matrix simulator[ref (38)]. One-qubit and two-qubit gates are applied to the density matrix as completely positive, trace preserving maps represented by Pauli transfer matrices. Moreover, the time of application occurs at the mid point in time of the gate. For example a 20 ns gate will be applied after an idling time of 10ns, which will then be followed by another idling time of 10ns. The idling time is when the qubit will be exposed to errors. The error model consists of qubit relaxation and dephasing, which are the dominant sources of error in superconducting qubits[ref (25)]. We will give the definitions of these quantities in chapter 4 on device characterization. The qubit relaxation times(T_1) are taken to be 10 and 11. The qubit Ramsey times(T_2^*) are taken to be 10 and 11. These numbers are taken from the device characterization reported in chapter 4. The length of single qubit gates is taken to be 20ns and the length of the iSWAP(θ) is taken to be 8ns. A detailed characterization of iSWAP(θ) is given in chapter 5. The angle θ of the iSWAP depends on its length in time, here 8ns corresponds to a fully entangling iSWAP, which occurs at $\theta = \pi/4$. We do not implement the tomographic pre-rotations for these simulations as we extract the density matrix after applying the circuit. We construct the energy of the Hydrogen Hamiltonian by calculating the expectation values of all pauli terms by using the born rule, given by the equation $\langle \hat{O} \rangle = Tr[\hat{\rho}\hat{O}]$. We use Nelder-Mead optimization algorithm for minimization of energy. It is important to note that we haven't incorporated any sampling noise which would occur in extracting expectation values in an experiment. This is done for simplicity in the simulations. We implement Hamiltonians at 54 different bond lengths, R across the dissociation curve. Additionally, we start the simulation for lowest Bond Length with a random starting guess for parameters, but when we go to the next distance we use the converged parameters of the last distance. It is possible to do so because the hydrogen dissociation curve is smooth and we expect the parameters of the wavefunction that minimize the energy for the next inter-atomic distance to be close to the converged parameters for the previous inter-atomic distance. This reduces the number of iterations needed to converge. Figure 3.2 (b) shows the converged energies for the entire dissociation curve which consists of 54 points, the minima of this curve occurs at 0.7 \AA consistent with the equilibrium bond-length of diatomic hydrogen. Figure 3.3(a) shows errors w.r.t to the ground state. The error in energy estimate by using PCA are quantitatively similar to that by using HOA, which is not reported here. This is because both these circuits have the same length in time.

3. NUMERICAL SIMULATIONS OF VQE ALGORITHM

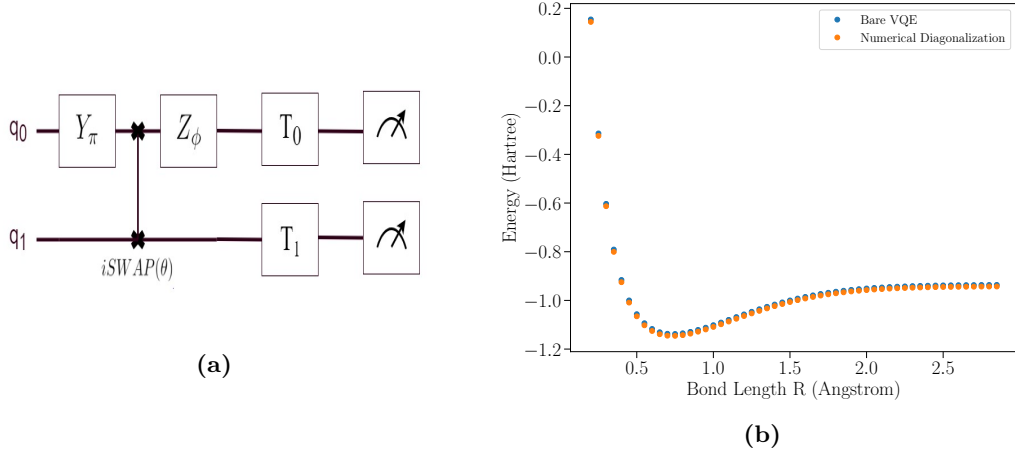


Figure 3.2: a. Quantum circuit for the particle number conserving Ansatz. The Z-gate and the swap are parameterizable. Measurement waiting gate is not shown but added to the simulation. b. Plot of Converged Energies(Hartree) across Bond lengths.

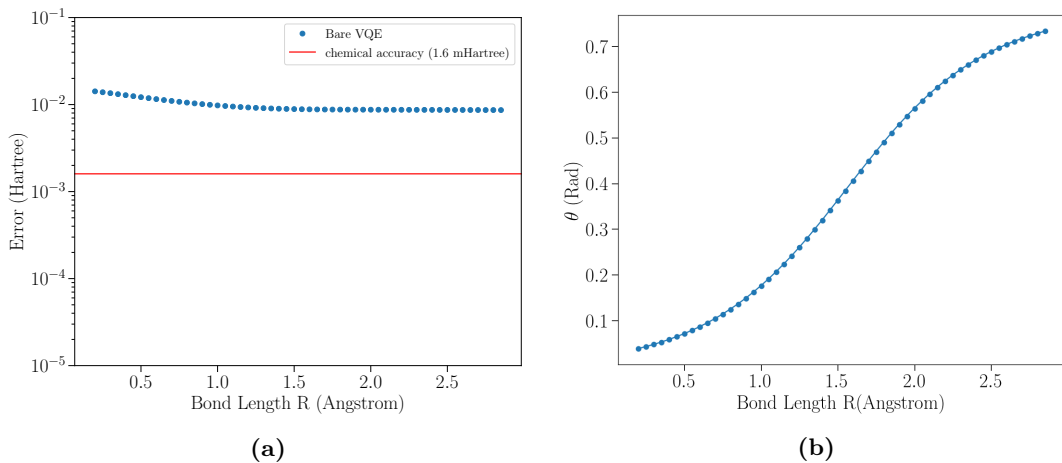


Figure 3.3: Error in energy estimate obtained by using PCA circuit(a), red line represents chemical accuracy. Errors are computed form the exact solution.b. Plot of iSWAP angle of the converged states(dots) and the exact solution(continuous line) across interatomic distances.

In figure 3.2(a) shows that we are an order of magnitude away from chemical accuracy. Since our error model for this simulation contains only T_1 and T_ϕ , we will attribute these errors almost entirely to these errors.

Figure 3.3(b) shows the converged angles of $iSWAP(\theta)$ gate, this is well in agreement with the angles calculated from theory(continuous line).

In chapter 6, where we discuss the experimental results we will see how simulations describe the errors in energy estimates obtained experimentally. We will take the circuit lengths the

same as used in experiment, which differ considerably from the circuit length used here due to the presence of buffers in our experimental circuit. However, the length of single and two-qubit gates will remain the same.

3.1 Error Signalling

Inaccuracies in the ground state estimate produced by the VQE are caused due several factors most prominent of them are inaccuracy in the design of state preparation Ansatz, qubit state decay due to limited relaxation time (T_1), decay of coherence due to limited dephasing time (T_2), single qubit gate errors, two-qubit gate errors and sampling noise in measurement of pauli terms. In this section we focus on combating errors introduced by qubit state relaxation. If during the preparation of the state in the odd parity subspace a T_1 decay event occurs, then the state is no longer in the odd parity subspace, i.e. upon parity measurement we will get a +1. In order for us to improve our energy estimate we must rule out states with an even parity while simultaneously measuring pauli terms in the hydrogen Hamiltonian. The hydrogen Hamiltonian is given by eqn.(2.10) and it commutes with the parity operator ZZ eqn(2.11). Moreover terms XX and YY also commute with the Hamiltonian. This is the first step in ensuring that terms in the Hamiltonian and parity of the state are simultaneously measurable. To measure the term $\langle XX \rangle$ we perform a two qubit Clifford rotation that takes $\langle XX \rangle$ and $\langle ZZ \rangle$ to separate qubits. The circuit is shown in Fig 3.4, top qubit (qubit q0) encodes the parity. After the state preperation step similar to particle number conserving circuit, we rotate both qubits to XX basis by applying $\hat{R}_{\hat{y}}(\frac{\pi}{2})$ on both qubits. We follow this with a CNOT gate compiled with a CZ- π gate and $Y_{\pm\frac{\pi}{2}}$ gates. We then bring one of the qubits back to the Z basis by using a $Y_{-\frac{\pi}{2}}$ rotation, upon measurement of this qubit we will extract the parity of the qubits. The other qubit is still in X basis and upon its measurement we extact XX. We employ postselection and average outcomes for the XX measurement only when odd parity measured on the other qubit(qubit q0). By this postselection scheme we eliminate most of the T_1 errors. The circuit in Fig 3.4 implements this Clifford rotation. We use similar insight to write down a circuit for YY measurement. For IZ, ZI and ZZ measurements which will come from simulataneous Z measurements on both the qubits(the correlation term will be extracted by multiplying the shots and averaging them), we can measure the parity trivially and remove them in software. In Fig 3.5 we see the reduction in error, we also see that the error increases as R increases. We attribute this to the transition from relaxation dominated to a dephasing dominated regime.

3. NUMERICAL SIMULATIONS OF VQE ALGORITHM

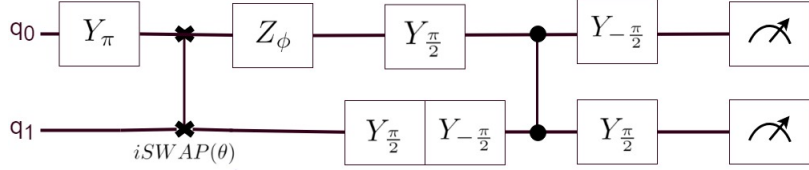


Figure 3.4: Error signalling circuit used to obtain the expectation value of XX operator. The rotations $Y_{\pi/2}$ and $Y_{-\pi/2}$ occurring next to each other are not compiled for clarity. The C-NOT gate is applied with qubit q0 as control and qubit q1 as target. It is compiled with a C-Phase.

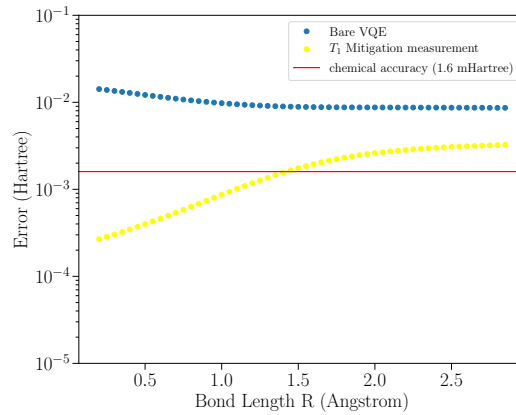


Figure 3.5: Error in energy estimate obtained after T_1 mitigation measurement.

This is because dephasing effects are more pronounced at higher bond lengths as ground states at higher bond lengths require higher entanglement in the prepared state.

3.2 Active Error Mitigation

Errors in VQE state preparation have the effect of increasing the measured expectation value of energy \tilde{E} from its true value E . In the presence of errors the prepared state will be better represented by an ensemble given by a density matrix $\rho(\theta)$. In the ideal case when preparation is error free $\rho(\theta) = |\psi(\theta)\rangle \langle \psi(\theta)|$. The ground state variational principle still exists[ref (17)] for all values of $\vec{\theta}$.

$$\langle \hat{H} \rangle_{\rho(\vec{\theta})} \equiv \langle \hat{H} \rangle(\vec{\theta}) = \text{Tr}[\rho(\vec{\theta}) \hat{H}] \geq E_{GS} \quad \forall \theta \quad (3.6)$$

We denote the minimized energy or the energy estimate as \tilde{E} and the error in energy estimate

3.2 Active Error Mitigation

as ϵ .

$$\min_{\forall \vec{\theta}} \langle \hat{H} \rangle_{\rho(\vec{\theta})} \equiv \tilde{E} \quad (3.7)$$

$$\epsilon \equiv | \tilde{E} - E_{GS} | \quad (3.8)$$

The basic idea behind active error minimization[ref (34), ref (28)] is that we want to have parameter(s) r which characterize the errors in our Energy estimation. We then find a functional relationship between the Energy estimate and the error parameter. We extrapolate this curve to $r \rightarrow 0$ and find $\tilde{E}(r \rightarrow 0)$. This technique works only for those errors in the state preparation which are stochastic, such that the operation is described by a super-operator $\hat{N}\hat{U}(\theta)$ and \hat{N} can be written as[ref (34)]:

$$\hat{N}_\lambda = (1 - \lambda)\hat{I} + \lambda\hat{E} \quad (3.9)$$

Where $\hat{U}(\theta)$ is the ideal unitary operator used to prepare the state ansatz, \hat{N} is a super-operator describing the effect of noise, \hat{I} is an identity operation and errors \hat{E} occur with a probability λ . Starting with an initial state $|0\rangle\langle 0|$, after n iterations of state preparation, the density matrix obtained is given by:

$$\rho_\lambda(\vec{\theta}_n) = \hat{N}_{n,\lambda}\hat{U}_n..\hat{N}_{1,\lambda}\hat{U}_1|0\rangle\langle 0| \quad (3.10)$$

Where the ideal unitary operator in the l^{th} iteration is given by $\hat{U}(\theta_l)$. Taking into account that the errors are stochastic, the minimized outcome of expectation value of the Hamiltonian can be written as:

$$\langle \hat{H} \rangle_{\rho_\lambda} = (1 - r \sum_l \lambda_l) \langle \hat{H} \rangle_{\rho^{(0)}}^{(0)} + r \langle \hat{H} \rangle_{\rho^{(1)}}^{(1)} + O(r^2) \quad (3.11)$$

Here, $\langle \hat{H} \rangle_{\rho_\lambda} = Tr[\hat{H}\rho_r(\vec{\theta})]$ and $\langle \hat{H} \rangle_{\rho^{(0)}}^{(0)} = Tr[\hat{H}\rho^{(0)}(\vec{\theta})]$ and $\rho^{(0)} = \hat{U}_n...\hat{U}_1$ i.e. the density matrix without any errors. $\rho^{(1)} = r \sum_l \lambda_l \hat{U}_n..\hat{E}_l \hat{U}_l..\hat{U}_1(|0\rangle\langle 0|)$ denotes the normalized sum of all state preparation density matrices in which only one of the operations causes an error, and all other operations are ideal. Note, that in these equations r is a scale factor and we have replaced the error probability λ_l with $r\lambda_l$ allowing us to write eqn(3.11) with r dependence on the right hand side. We will use r instead of λ as an error parameter. The value $\langle \hat{H} \rangle_{\rho^{(0)}}^{(0)}$ is the true value of energy estimate and can be obtained by the means of extrapolation[ref (33)]. The eqn(3.11) can be rewritten as:

$$\langle \hat{H} \rangle_{\rho_r}^{(0)} = \langle \hat{H} \rangle_{\rho^{(0)}}^{(0)} + \chi r \quad (3.12)$$

3. NUMERICAL SIMULATIONS OF VQE ALGORITHM

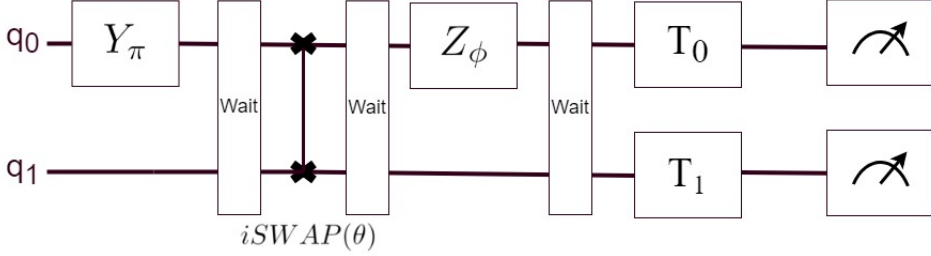
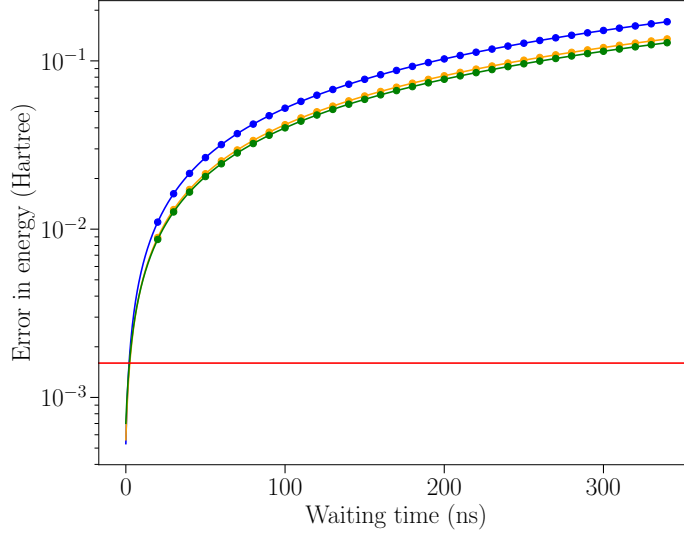


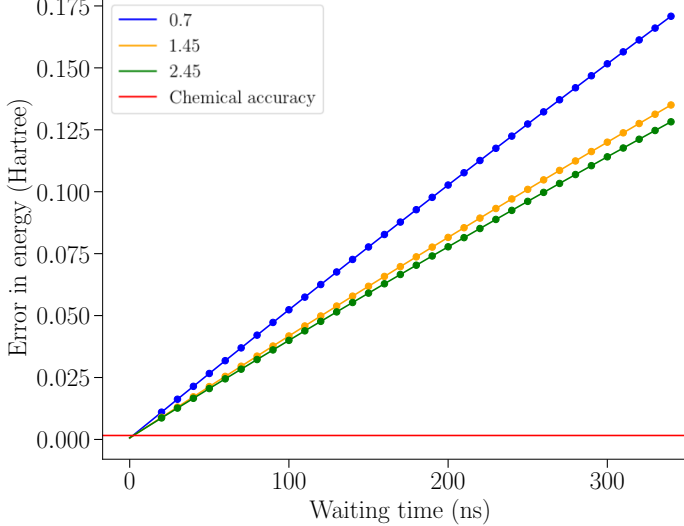
Figure 3.6: Quantum circuit used in the AEM protocol. A waiting gate is inserted after every single and two-qubit gate operations. T_0 and T_1 represent tomographic pre-rotations.

Where $\chi = \sum_l \lambda_l \left\langle \hat{H} \right\rangle_{\rho^{(0)}}^{(0)} + \left\langle \hat{H} \right\rangle_{\rho^{(1)}}^{(1)}$ In our experiments the error parameters r cannot be less than r_{min} therefore to access the true value of energy estimate, we increase r and extrapolate energy estimate to $r = 0$.

To ascertain the usefulness of the active error minimization protocol we begin by constructing a protocol to tune out errors introduced in our circuit by finite decay and pure dephasing characterized by T_1 and T_ϕ respectively. In our experiments it is not feasible to change either of these numbers. But since total errors per evaluation of the circuit is just an integration of the rate of errors over time of exposure, so we instead change the circuit length by adding waiting gates(Fig 3.6) after every gate operation thereby changing the time for which our system is exposed to decoherence. This assumption is not quite true in practice as T_2 changes when we flux pulse a qubit out of its sweetspot, but to move ahead we make the assumption that T_2 stays constant throughout the entire circuit execution. We obtain error in energy estimation for three points on the dissociation curve for several values of waiting time(Fig 3.7). The total circuit length which becomes our parameter "r" is related to waiting times by the equation $r = \text{native circuit length} + 3 \times \text{wait time}$. The single qubit and two qubit gate lengths of 20 and 8ns respectively, as before. We observe an increase in the errors with increasing circuit length as expected(Fig 3.7(a),(b)). We added the waiting gates in steps of 10 ns. The x-axis of Figure 3.7(a),(b) is the length of single qubit gate plus waiting time added. The total waiting time is a factor of 3 of this length. Fig 3.7 shows error as a function of waiting time with a polynomial fit in both log and linear scale, so that the reader can appreciate both the extrapolated error and the approximately linear dependence on waiting time. The fit used was a third degree(cubic) least squares fit, where the coefficients of third and second degree are very small compared to the first degree coefficient. If only the first few waiting times are chosen the error dependence



(a) Log-scale.



(b) Linear scale.

Figure 3.7: Error in energy estimate as a function of waiting time (dots). The total circuit length is three times the waiting time. Continuous lines depict a least squares fit to a third-order polynomial.

becomes linear.

In Fig 3.8 we look at errors in energy estimation for the Hydrogen Hamiltonian after obtaining extrapolations for the entire dissociation curve. The extrapolated error is called the zero noise limit[ref (28)] as it corresponds to the hypothetical case in which all gate op-

3. NUMERICAL SIMULATIONS OF VQE ALGORITHM

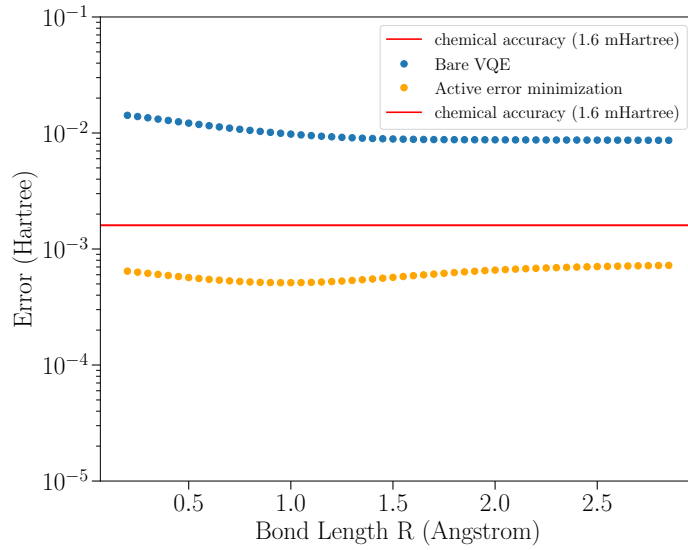


Figure 3.8: Error in energy estimate after applying active error Minimization. Also shown for comparison is the Bare VQE error curve. The extrapolated error(orange) is approximately an order of magnitude lower.

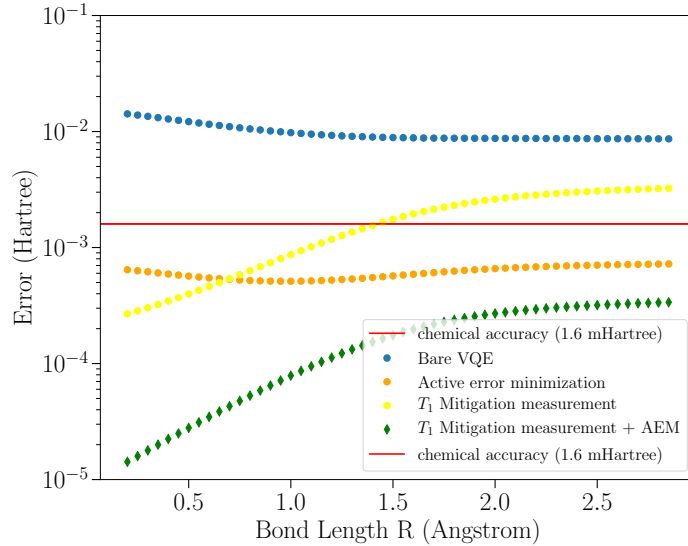


Figure 3.9: Error in energy estimate obtained after applying Active error Minimization on top of T_1 mitigation measurement(green diamonds). Also shown for comparison is the Bare VQE error curve(blue), T_1 mitigation measurement (yellow) and AEM(orange).

erations were performed instantaneously so that there was no exposure to decoherence during them, and these operations had no additional errors. We see a considerable improvement in our energy estimate(orange dots in Fig 3.8) for the entire dissociation curve in comparison to bare

3.2 Active Error Mitigation

VQE(blue dots in Fig 3.8). We must emphasize that our error model is limited to decay and pure dephasing, which is a crude approximation. We will discuss the limitations of the simulations briefly in the last section. We can easily combine active error minimization with parity verification by obtaining refined error estimates from the parity verification at every waiting time step. In Fig 3.9 we plot the errors for all techniques covered in this chapter so far. We see that by combining AEM with parity verification we can estimate our energy to below chemical accuracy benchmark. These simulations were done after characterizing the device and used to assess the potential of our device for accurate quantum simulations. In the next section we describe a more efficient way of doing T_1 mitigation by simple rescaling of obtained expectation values.

3. NUMERICAL SIMULATIONS OF VQE ALGORITHM

3.3 T₁ mitigation by rescaling in post-processing

A more efficient way to mitigate T₁ errors is by expressing the expectation values of Pauli operators for a density matrix lying in the protected parity subspace(ρ_P) in terms of the expectation values of the density matrix that does not lie in the protected subspace(ρ)[ref (37)]. As a starting point, we set the expectation values of all operators that anti-commute with the Hamiltonian to 0. The density matrix in the protected subspace, ρ_P is given by

$$\rho_P = \frac{\frac{1}{2}(1-P)\rho}{Tr[\frac{1}{2}(1-P)\rho]} \quad (3.13)$$

And the expectation values of the commuting operators for the state ρ_P expressed in the terms of expectation values of ρ are

$$Tr[\sigma\rho_P] = Tr\left[\sigma\frac{\frac{1}{2}(1-P)\rho}{Tr[\frac{1}{2}(1-P)\rho]}\right] = \frac{Tr[\sigma\rho] - Tr[\sigma P\rho]}{1 - Tr[P\rho]}. \quad (3.14)$$

The operators occurring in the Hamiltonian all commute with the Hamiltonian and can be expressed as:

$$\begin{aligned} \langle IZ_{mit} \rangle &= \frac{\langle IZ \rangle_{exp} - \langle ZI \rangle_{exp}}{1 - \langle ZZ \rangle_{exp}} \\ \langle ZI_{mit} \rangle &= \frac{\langle ZI \rangle_{exp} - \langle IZ \rangle_{exp}}{1 - \langle ZZ \rangle_{exp}} \\ \langle ZZ_{mit} \rangle &= \frac{\langle ZZ \rangle_{exp} - 1}{1 - \langle ZZ \rangle_{exp}} = -1 \end{aligned} \quad (3.15)$$

$$\begin{aligned} \langle XX_{mit} \rangle &= \frac{\langle XX \rangle_{exp} + \langle YY \rangle_{exp}}{1 - \langle ZZ_{exp} \rangle} \\ \langle YY_{mit} \rangle &= \frac{\langle XX \rangle_{exp} + \langle YY \rangle_{exp}}{1 - \langle ZZ_{exp} \rangle} \end{aligned} \quad (3.16)$$

This technique has the advantage of no overhead in the circuit and can be implemented entirely in post-processing. We will discuss the numerical simulations of this technique in the chapter on experimental results and compare it to experimental data.

3.3.1 Limitations of the simulations

Following are the limitations of the simulations performed:

- We only use T_1 and T_ϕ as the mechanisms for error. This is not true as our single and two qubit gates will introduce additional errors in the VQE[ref (38)].
- Another mechanism of error arises from sampling noise. Here we have extracted the values of pauli terms occuring in the Hamiltonian by first extracting the denisty matrix and then using the formula $\langle \hat{O} \rangle = Tr[\hat{\rho}(\theta)\hat{O}]..$.
- We have not taken into account the dephasing and decay that occurs during the measurement. This is because we will do tomography using an overcomplete set, to reconstruct the density matrix. In the simulations presented in the outlook section we assume that this technique will get rid of the decay and dephasing that occurs during the measurement.

At the end we assert that our simulations are only indicative of the improvement in energy estimate in a real experiment.

3. NUMERICAL SIMULATIONS OF VQE ALGORITHM

4

Device Characterization

In this chapter we introduce and report the characterization of the device that will be used to test the protocols that we have developed in collaboration with the theory team comprising of Thomas O'Brien and Xavier Monorig. The chip(Fig 4.1) is a 3-qubit Transmon[ref (27)] processor, designed and fabricated by Ramiro Sagatzizabal with help from fab team comprising of Alessandro Bruno and Nandini Muthusubramanian. The three qubits are named Data top(D1), Data bottom(D2) and Ancilla(A), the connectivity is of the form D1-D2-A, where dashes are the bus resonators.

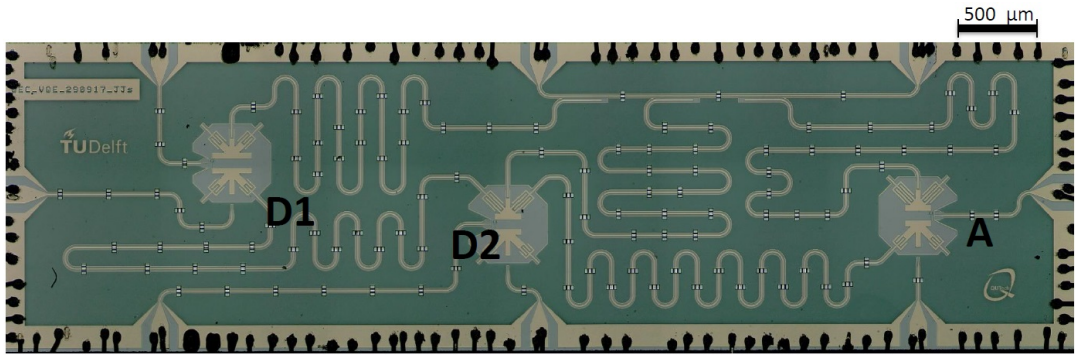


Figure 4.1: Three Qubit Transmon quantum processor. Qubits A and D2 will be used in the experiments.

Several devices were fabricated and on the basis of room temperature Two-Probe Voltage measurements candidates for a cooldown were selected. The data from the Voltage measurements was used to extract the resistance of the Josephson Junction(R), using the formula $R_J = 1000/\text{Voltage}$. The Joshepson energy(E_J) is given by $\frac{M[\text{GHz} \cdot k\Omega]}{R}$, where M is the magic number. The Josephson charging energy (E_c) is taken to be 268.4 MHz, on the basis of previ-

4. DEVICE CHARACTERIZATION

ous experiments. From, these numbers we estimate the ground state to excited state transition frequency ω_{01} for all qubits across all device samples using the formula

$$\omega_{01} = \sqrt{8E_c E_J} - E_c \quad (4.1)$$

We also estimate the ratio of E_J/E_C to estimate where (and if at all) in the Transmon regime our devices are. Basis on these two numbers and difference in the qubit frequencies in each device we make the choice for the candidate device.

4.1 Continuous-wave measurements

4.1.1 VNA Scans for resonators

In context of the measurements we do to characterize the device, the only information we can get out of it comes from the transmission measurements of the feedline, through which the qubits are capacitively coupled. We start with a broad scan covering the frequency region of interest, based on targeted readout-resonator frequencies. When the qubit is coupled to a resonator, the energy levels of one are influenced by the other.

The coupling between qubit and resonator denoted by g , determines the rate at which they can exchange excitations. The difference between the qubit frequency ω_{01} and the bare resonator frequency ω_r is given by the detuning $\Delta = \omega_{01} - \omega_r$. If the magnitude of detuning is large compared to the coupling strength, the system is in the dispersive regime. In this case the qubit-resonator Hamiltonian can be approximated by the dispersive Jaynes-

Cummings Hamiltonian:

$$\hat{H} = \frac{\hbar\omega'_{01}}{2}\hat{\sigma}_z + (\hbar\omega'_r + \hbar\chi\hat{\sigma}_z)\hat{a}^\dagger\hat{a} \quad (4.2)$$

Where $\omega'_{01} = \omega_{01} + \chi$, $\omega'_r = \omega_r - \frac{\chi}{2}$ are the dressed qubit and resonator frequencies. The dispersive shift χ is given by the equation

$$\chi = \frac{g^2}{\Delta} \frac{E_C}{\hbar\Delta - E_C} \quad (4.3)$$

The frequency shift of the resonator is seen only at low RF power where Jaynes-Cummings approximation is true [ref (25)].

4.1.2 Resonator Powersweep

Once the resonators have been located, the next step is to locate the qubit frequency. As the number of photons in the resonator reaches a critical limit, the resonator experiences a non-linearity, so it loses its Lorentzian lineshape. The system can no longer be approximated by Jaynes Cummings hamiltonian. When RF power is increased even further, at a certain point the resonator enters high power regime thereby regaining its Lorentzian lineshape, also the resonator comes to its bare frequency.

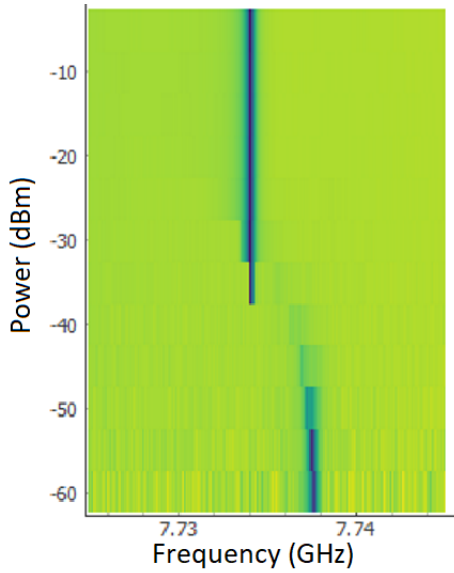


Figure 4.3: A powersweep of the resonator. $\omega = 7.7341$ GHz and $\omega = 7.7376$ GHz. The powershift is 3.5 MHz for this resonator.

During this powersweep the resonance frequency of the resonator goes from ω'_r to ω_{bare} . Observing this frequency shift means that the qubit is coupled to the resonator. Since the resonator frequency shifts downwards when going from low power to high power regime ($\omega_{bare} < \omega'_r$), this means that $\chi < 0$ and from eqn 4.3 $\Delta < 0$ and hence the qubit lies below the resonator.

4. DEVICE CHARACTERIZATION

4.1.3 Resonator DAC arches

After determining the powershift, which essentially tells us that there is a non-linear system coupled to our resonator that dresses it in low power regime. The next step is to see if the resonator frequency moves when a flux bias is applied to the qubit. We see in Fig 4.4 the resonator that moves the most when flux bias is applied through the FBL of A.

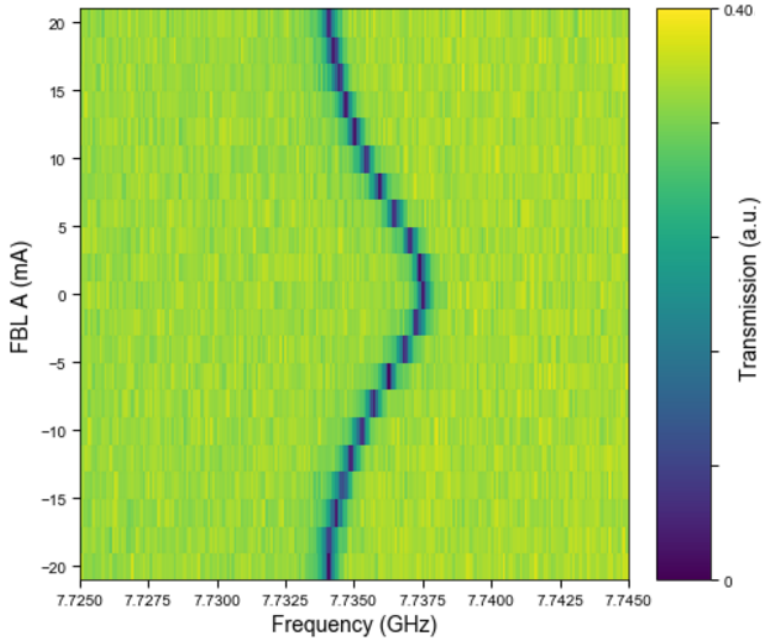


Figure 4.4: Resonator DAC arch for the resonator that responds the most to flux bias on qubit A.

Since the transmon frequency changes with flux as given in eqn (5.4) later, this changes

4.1.4 Two Tone Spectroscopy

As explained in section 4.1.1, the resonator undergoes a frequency shift of 2χ dependent on the state of the qubit. For a resonator capacitively coupled to the feedline, the transmission through the resonator is low when the qubit is in ground state and high when the qubit is in excited state. In Two Tone Spectroscopy(TTS) this property is exploited, by sending two tones:

- A driving tone with varying frequency ω_d . This is the qubit spectroscopy tone.
- A readout tone at the resonator frequency(when the qubit is in ground state).

We go through a few iterations of changing the power of the drive tone(Qubit spec power), until only prominent peak is visible. In Figure 6.4 we report a TTS of qubit A, with a RO power of -60 dbm(on the source) and qubit spec power of -55 dbm(on the source). The qubit peak is identified at

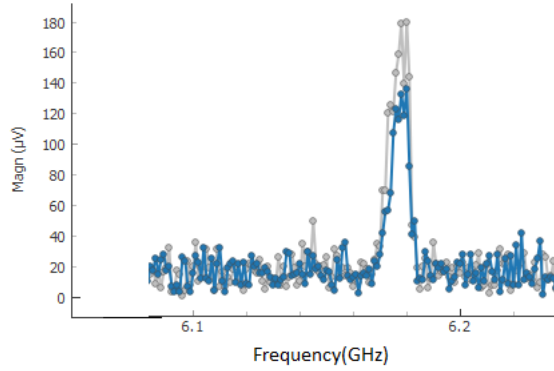


Figure 4.5: Two tone spectroscopy of qubit A at zero flux bias.

4.1.5 Tracked qubit spectroscopy

For flux tunable qubits such as ours we need to determine how the frequency of the qubit changes with flux[ref (27)].

$$E_J(\Phi) = E_J^{eff} \cos\left(\pi \frac{\Phi}{\Phi_0}\right) \quad (4.4)$$

where $\Phi_0 = h/2e$ is the magnetic flux quantum and Φ is the flux passing through the squid loop. For symmetric squids the E_J^{eff} is given by $2E_J$.

$$\hbar\omega_{01} = \sqrt{8E_J(\Phi)E_C} - E_C \quad (4.5)$$

The tracked spectroscopy is simply two-tone spectroscopies done with varying DAC values, such that the qubit frequency measured in a previous scan is extrapolated to find the frequency window used for searching the qubit. Additionally in every new iteration the resonator is found again, as moving the qubit also moves the resonator. In Figure 4.6 we report such a Tracked Spectroscopy done overnight for Qubit A. The maximum of the curve gives us the qubit sweetspot. This occurs at 19.816 mV, the qubit frequency at the sweetspot is 6.1793 GHz.

4. DEVICE CHARACTERIZATION

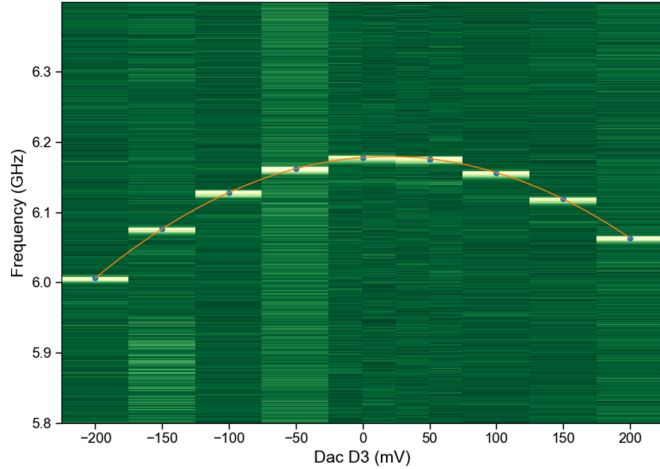


Figure 4.6: Tracked spectroscopy of qubit A with FBL of A (D3 on the plot)

4.1.6 Avoided Crossing

Our device has a connectivity of the form D1-D2-A, where dashes are the bus resonators. Since the qubit A is coupled to D2, when qubit A is moved by fluxing into resonance with qubit D2, their energy eigenstates hybridize and hence cannot cross. This hybridization of energy levels gives rise to two frequency peaks at the flux(on A) which brings qubit A in resonance with qubit D2.

In figure 4.7 we report the $|ge\rangle \leftrightarrow |eg\rangle$ avoided crossing between qubit A and D2. The resonator mediated coupling $\frac{J_1}{2\pi}$, is found out to be 20.9 MHz. We will give more details on this in section 5.4.1.

4.2 Time Domain Measurements

4.2.1 Qubit relaxation: T1

Qubit Relaxation is caused by the exchange of energy between qubit and the environment. It causes an excited state to decay to ground state after a finite time. To be precise environmental degrees of freedom that cause a perturbation perpendicular to the quantization axis, eg. fast charge fluctuations contribute to relaxation. To measure T_1 a π pulse is applied to put qubit into an excited state. After waiting for a variable time τ , the state of the qubit is measured and probability of it being in excited state is calculated. After being put into the excited state the qubit, the qubit has a probability described by an exponential decay $1 - \exp\left(-\frac{\tau}{T_1}\right)$ of

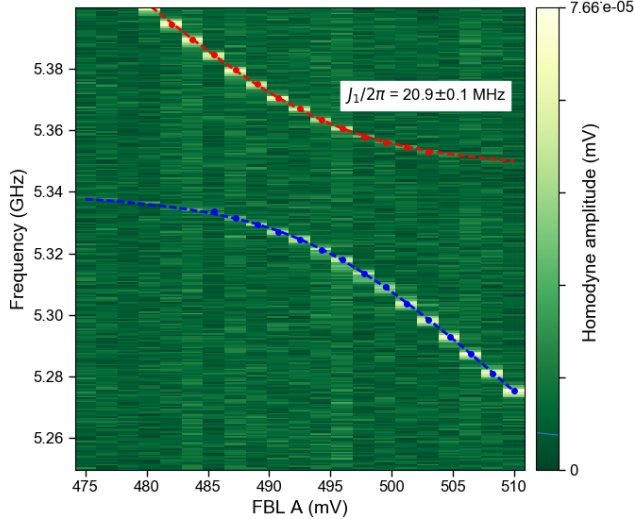


Figure 4.7: Avoided Crossing between $|ge\rangle$ and $|eg\rangle$ states

remaining in excited state. In a T_1 measurement the excited state probability is plotted against the variable wait time τ , this is fit to the exponential decay and T_1 is estimated.

4.2.2 Qubit dephasing: Ramsey

Next, we consider dephasing which results from phase noise. Phase noise can be seen as fluctuations in qubit frequency which results in random accumulation of phase over time. If we start with an ensemble of pure states along the equator of the Bloch sphere, then the random accumulation of phase will cause all the initial phase information to be lost, the ensemble after a long enough time will be a purely mixed state located at the center of the Bloch sphere.

The amount of dephasing is characterized by T_2^* and its upper bound is $2T_1$ due to the fact that T_1 errors also cause dephasing. Measuring the dephasing time T_2^* is done by a Ramsey measurement. It consists of an initial $X_{\frac{\pi}{2}}$ pulse, after which the qubit lies on the equator of the Bloch sphere. After a certain wait time τ , a second $X_{\frac{\pi}{2}}$ pulse is applied to the qubit. The combination of the two pulses should put qubit in the excited state, but the qubit experiences dephasing during the wait time τ and it's state deviates from the excited state. The probability of the final state to end up in the excited state has an exponential decay, asymptotically approaching 0.5(all phase information lost or purely mixed state). The driving tone ω_d is detuned from the qubit frequency ω_q , as a result the qubit acquires a phase with respect to the rotating frame of the drive at a rate given by $\omega_d - \omega_q$. Due to this precession

4. DEVICE CHARACTERIZATION

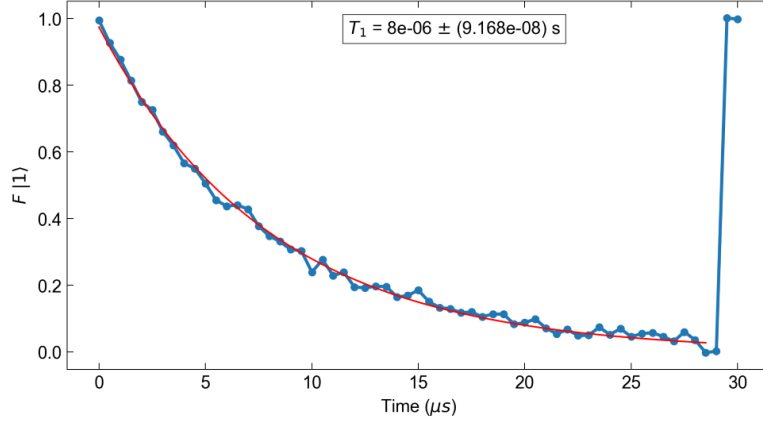


Figure 4.8: T_1 measurement with an exponential fit. The last 4 points are taken for calibration of probabilities.

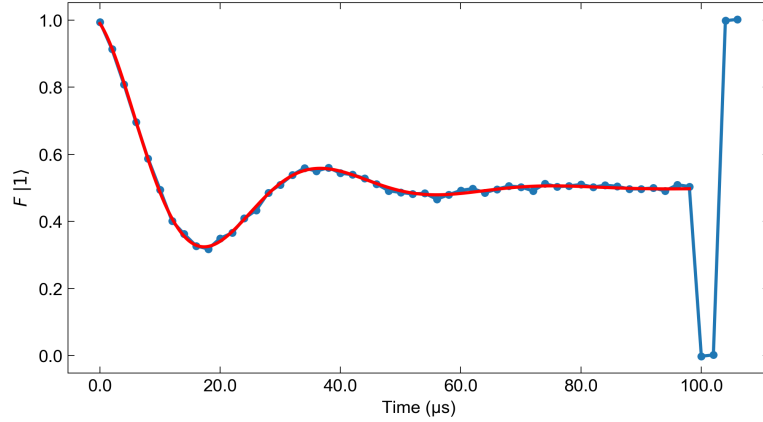


Figure 4.9: Ramsey measurement with a decaying cosine fit, $T_2^* = 17.73\mu\text{s}$. This data was taken in a cooldown different to the one in which the VQE experiments were performed. For complete qubit spec table please refer to the last section of this chapter.

the Ramsey measurement also exhibits an oscillation. This is done to make the fit better and these oscillations can help refine the qubit frequency estimate. Fig 4.9 reports the results of a Ramsey experiment done on qubit A.

4.2.3 Fast frequency qubit dephasing : Echo

The dephasing time T_2^* has contributions from both high frequency noise and low frequency noise. It is possible to assess which source is the dominant one using an Echo sequence which filters out slow noise. An Echo sequence is created by embedding a refocusing X_π pulse in the

middle of the variable wait time τ between $X_{\frac{\pi}{2}}$ pulses. The phase noise that is slow compared to τ can be viewed as being quasi static and will be cancelled because of the flipping.

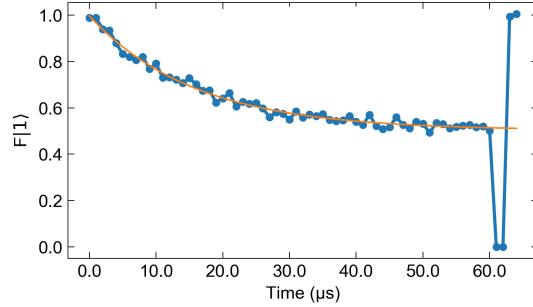


Figure 4.10: T_2^{echo} measurement, with a decaying exponential fit. The fit reported an echo time of 15.8. This data was taken in a cooldown different to the one in which the VQE experiments were performed. For complete qubit spec table please refer to the last section of this chapter.

Fast phase noise will still randomize the phase during τ and hence will dephase the qubit. Important to note here is the fact that the final state of the qubit is the ground state in the absence of decoherence, which is in contrast to the Ramsey measurement where the final state is the excited state. Also in the echo measurement if the ω_d is detuned from ω_q for both $X_{\frac{\pi}{2}}$ pulses we would still not see an oscillatory behaviour as the flipping pulse would cancel out the precession. We artificially shift the phase of the second $X_{\frac{\pi}{2}}$ pulse, which results in an artificial oscillation. This done to allow for better estimation of T_2^{echo} via fitting and clearer distinguishability of any spurious shapes in the measurement results.

4. DEVICE CHARACTERIZATION

4.3 Qubits Summary

Qubit	D1	D2	A
Measured seat-spot frequency(GHz)	4.2205	5.2265	6.0019
Measured sweet-spot(mA)	-0.401	-0.386	0.396
FBL coupling(mA/ Φ_0)	58.8	50.8	42.3
T_1 at sweet-spot(μ s)	35	9.4	9.8
T_2^* at sweet-spot(μ s)	16-19	10.4	10.8
T_2^{echo} at sweet-spot(μ s)	47	10.6	12.7
$\frac{J}{2\pi}$ (MHz)	-	11.3	20.9
E_C (MHz)	278.3	255.8	264.0
E_J (MHz)	9.169	15.01	20.32

5

Experimental Methods

5.1 Control Electronics Stack

The control electronics stack used in the Variational Quantum Eigensolver experiments consists of three main instruments, a central controller(CC-light), two modules of arbitrary waveform generators (QWG) and an ultra high frequency lock-in amplifier (UHFLI)[ref (30)].

The central controller (CC-Light) delivers triggers to the QWG and UHFLI, thereby by orchestrating the delivery of microwave pulses, flux pulses and measurement pulses to the qubit chip. For brievity we explain the functions of instruments below

1. Central Controller(CC-Light) : A digital device built with an Intel Altera Cyclone V SOC Field Programmable Gate Array (FPGA) chip. It supplies bit-strings, called as codewords(depicted by dashed lines in Fig 5.1) to slave devices listed below.
2. Qutech waveform generator-microwave(QWG-MW): The QWG-MW generates In-phase(I) and Quadrature(Q) components of single-qubit pulses upon receiving codeword trigger from CC-Light. Each codeword is assigned a numerical waveform (Voltage as a function of time) in its QWG. The I and Q components are mixed with a Local oscillator to prepare qubit pulses. Every module of QWG-MW has 4 channels. We use a single module to generate two I,Q pairs to prepare single-qubit pulses for 2 qubits.
3. QWG flux: The Qutech Waveform Generator-flux generates a fast flux pulse used for implementing two-qubit gates upon receiving a codeword trigger from the CC-Light. Similar to QWG-microwave, QWG-flux plays a waveform when triggered. We use one port of a single module to generate fast-flux pulse for one qubit.

5. EXPERIMENTAL METHODS

Text

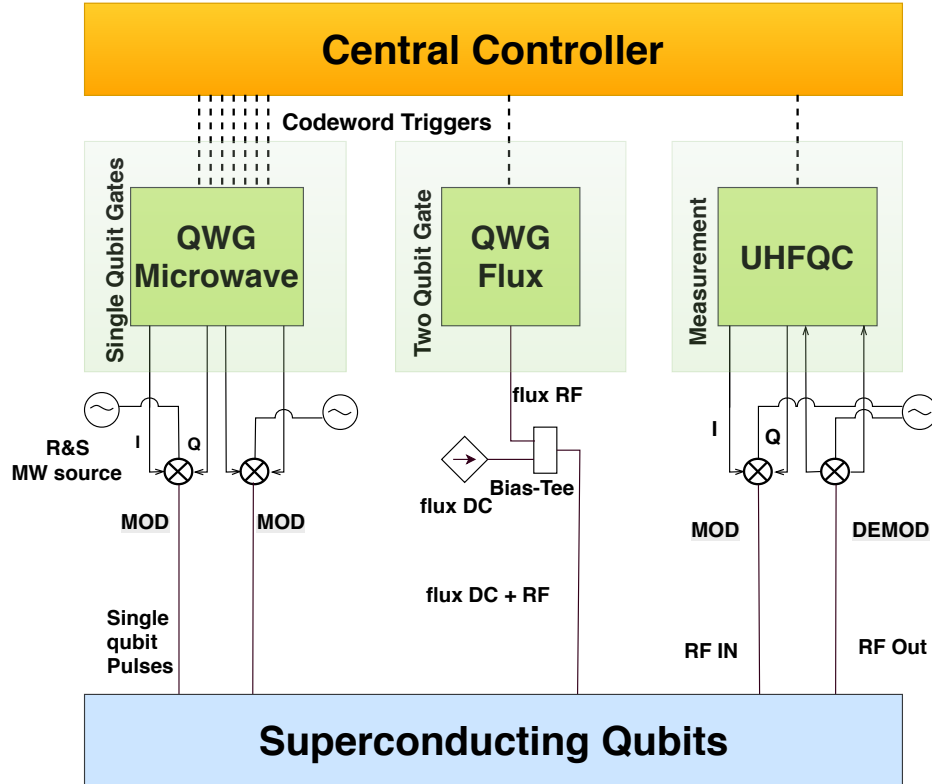


Figure 5.1: Control Electronics stack used in the VQE experiments. Dashed(continuous) lines represent digital(analogue) signals. Central Controller(orange) delivers codeword triggers to the QWG- microwave(used for single qubit rotations), QWG-flux(used for two qubit gates) and the UHFQC(used for measurement).

4. Ultra-High Frequency Lock-in Amplifier(UHFLI) or Ultra-High Frequency Quantum Controller(UHFQC): The UHFQC implements the measurement discrimination unit. It produces a frequency multiplexed pulse at the analogue signal output upon triggering. This pulse is mixed with a carrier wave and goes into feedline input (RF in in Fig 5.1). We measure the state of the qubit by probing the transmission through feedline. The transmitted signal(RF out in Fig 5.1) is demodulated and the I and Q components go into the analogue signal input of the UHFLI. The analogue ports operate at 1.8 GSa/s. The input and output signals are phase-locked.

Central Controller is programmed in openQL[ref (30)]. All experiments that are described in the next two chapters can be called codeword based event control schemes. We use the OpenQL

which is an open source programming language to program operations such as initialization by waiting, single-qubit gates, two-qubit gates, measurements and waiting times. An OpenQL program is essentially a sequence of these operations. The above control electronics stack is based on the codeword triggered paradigm of quantum computation experiments which is being actively pursued in the DiCarlo lab.

5.2 Single-Qubit gates

In Transmon qubits resonant microwave pulses are used to drive transitions between the qubit states[ref (1)]. The Hamiltonian of the driven qubit is given by

$$\hat{H} = -\frac{1}{2}\hbar\omega_{01}\sigma_z + \hbar\Omega_R \cos(\omega_d t + \phi)\sigma_x. \quad (5.1)$$

In the resonant case the drive frequency ω_d is equal to the fundamental frequency ω_{01} of the transmon qubit. The drive induces Rabi oscillations with a frequency Ω_R , depending on the strength of the drive. The phase of the drive ϕ sets the axis of single-qubit rotation on the Bloch sphere. Only single-qubit rotations whose axis lie on the equatorial plane of the Bloch sphere are possible in this way. IQ modulation is used to accurately control the envelope and phase of the pulse. The in-phase(I) and the quadrature(Q) components of the pulse are generated by QWG MW, as has already been mentioned in the previous section. The I and Q pulses produced by the QWG are at an intermediate frequency of 100 Mhz. This pulse is then modulated by a carrier wave at microwave frequency produced by a Rohde Schwarz SGS 100A RF source. To minimize leakage to state outside computational basis we use the Derivative Removal by Adiabatic Gate (DRAG) technique[ref (14)]. Calibrating the single-qubit gates requires us to tune the drive amplitude, qubit frequency, the motzoi parameter and $\frac{\pi}{2}$ amplitude scale. To ascertain the precision of our calibrations we do an ALLXY measurement. This consists of all twenty one possible two gate combinations taken from the set $\{\mathbb{1}, X_\pi, X_\pi, X_{\frac{\pi}{2}}, X_{\frac{\pi}{2}}\}$. Each gate combination is susceptible to a different type of error giving rise to error syndromes. The gates are arranged in such a way that the first 5 combinations For a detailed analysis of error syndromes see ref [ref (41)]. In Fig 6.1(a) we report a tuned ALLXY measurement of qubit D2 on our chip. The tuning was done right before a typical VQE experiment.

Next, we characterize gate errors with high accuracy using the Randomized Benchmarking(RB) protocol[refs (11),(12)]. The RB protocol consists of repeated application of gates drawn randomly from a set of unitary operations, after which the qubit fidelity to the theoretical final state(in the absence of gate errors) is measured. This can be translated to average

5. EXPERIMENTAL METHODS

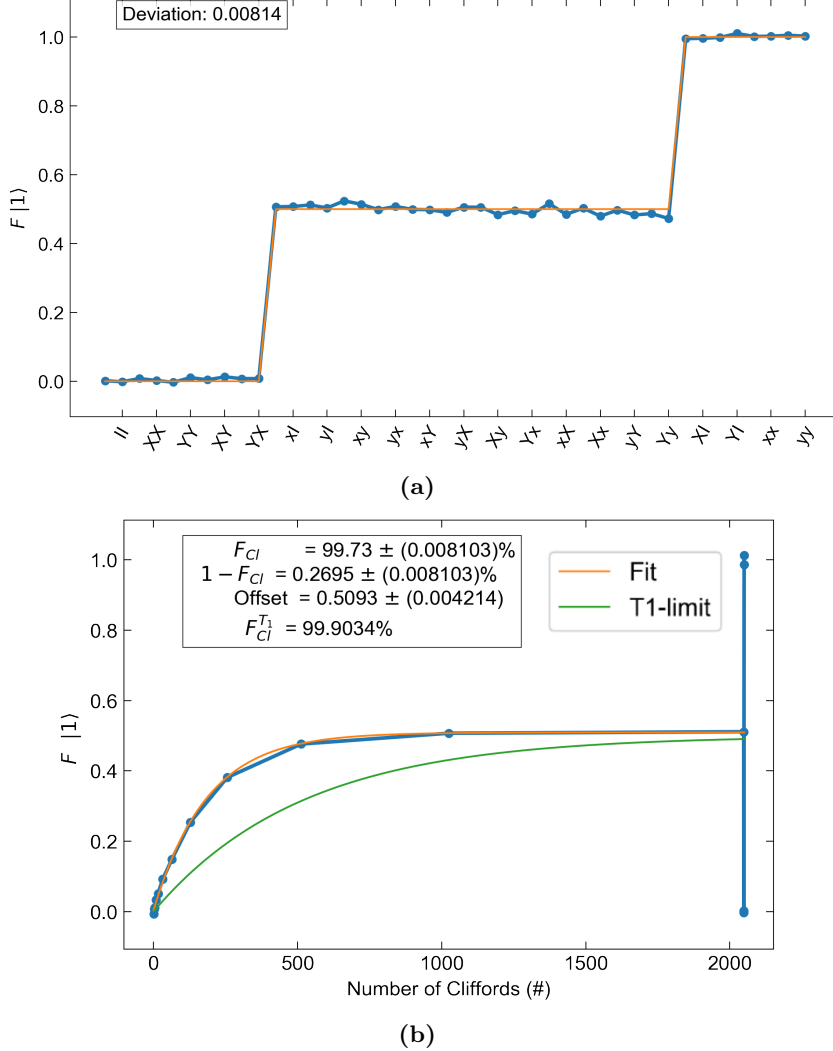


Figure 5.2: Fidelity of Single-Qubit gates. (a) Results of an ALLXY experiment after a tuneup. On the x-axis, lowercase represents $\frac{\pi}{2}$ rotations. (b) Results of a single-qubit Randomized Benchmarking experiment after a tuneup. We achieve a single qubit clifford gate fidelity of 99.73%. In this qubit, the fraction of error caused by qubit relaxation ($1 - F_{CL}^{T_1}$) over total error ($1 - F_{CL}$) is 35.77%.

error per operation. We perform a single qubit RB for which we draw the gates from the set of single-qubit Clifford group, \mathcal{C}_1 . The single-qubit Clifford group is the set of unitary transformations on the single-qubit Pauli group, $P_1 = \{\mathbb{1}, X, Y, Z\}$. \mathcal{C}_1 has 24 elements. Each of the Cliffords in \mathcal{C}_1 can be decomposed into rotations along X and Y axis. For details on the decomposition please refer to [ref (2)]. Following is the protocol we follow:

1. Initialize the qubit to a ground state, $|0\rangle$.
2. Apply n consecutive cliffords (C_1, \dots, C_n) where $C_i \in \mathcal{C}_1 \forall i \in \{1, \dots, n\}$.
3. Apply inverting Clifford $C_{inv} = (C_n \dots C_1)^{-1}$.
4. Measure the state of the qubit.

In Fig 5.2 (b), we plot Fidelity to excited state($F|1\rangle$)as a function of number of Cliffords (n). It is related to the ground state population by $P_0 = 1 - F|1\rangle$. The ground state population follows an exponential decay of the form

$$P_0 = \frac{1}{2}p^n + \frac{1}{2}. \quad (5.2)$$

Where p is an exponential decay parameter related to the average fidelity per operation by $F_0 = \frac{1+p}{2}$. In our fits we use a more detailed model of an exponential. The offset reported in Fig 5.2 (b) replaces the second half in the eqn 5.2. By using the number of gates per operations n_g , average fidelity per clifford is given by $F_0^{n_g^{-1}}$. The maximum fidelity is bounded by the T_1 limit arising from the qubit relaxation. it depends on the gate duration t_g [ref (43)]. In Fig 5.2(b) we report the results after a typical tuneup. We see that we are not at the T_1 limit. Errors due to T_1 constitute only 35.7% of total error. The other qubit had similar single qubit gate fidelities. For, the VQE experiments this means that our error model, which only consists of T_1 and T_2 will not account for the two-thirds of the error that occur during a single qubit gate. However, we do not yet have accurate information to model these errors in numerical simulations, hence we cannot make quantitative statements about by how much will these errors affect our energy estimate. The error can be further reduced by using the restless technique described in [ref (19)].

5. EXPERIMENTAL METHODS

5.3 Tomography

We use digitized measurements in the VQE experiments. For two qubits there are three sets of measured values. One set for each qubit that stores the digitized measured outcomes of that qubit. The third set stores the digitized correlation of the two qubits. We refer to these three sets as three channels. In order to evaluate energy we need to calculate the expectation values of pauli terms for a given prepared state. In this section we briefly describe Linear Least Squares tomography[ref (26)] in which we calculate expectation values of two qubit pauli operators from measurements on the readout resonators. We have access to digitized measurements of both qubits and their correlation as described in the section on multiplexed readout. Assume we have a general n-qubit state described by a density matrix $\rho \in \mathcal{H}^{d^2}$, where $d = 2^n$. We can then define an orthonormal basis set $P = \{\vec{p}_i, i = 1...d^2\}$, where \vec{e}_i are the basis vectors. The decomposition of ρ in this basis set is given by

$$[\rho]_P = \sum_{i=1}^{d^2} \rho_i \vec{p}_i \quad (5.3)$$

Quantum state tomography is then a procedure for estimating $d^2 - 1$ independent basis coefficients $[\rho_i]_P = \langle \vec{p}_i \rangle$ of ρ in P, where we have reduced the number of estimates needed by one due to $Tr[\rho] = 1$ constraint. We choose the Pauli basis set given by $P = \{\mathbb{1}, X, Y, Z\}^{\otimes n}$. The procedure essentially involves constructing a set of k measurements corresponding to known measurement operators $\{\hat{M}_j, j = 1...k\}$. If this set spans the space, we can obtain ρ by solving a linear system that arises from $m_j = Tr(M_j \rho)$. The first step in tomography is preparing the four computational basis states ($|00\rangle, |01\rangle, |10\rangle$ and $|11\rangle$) and calibrating the measurement operators of each channel[ref (26)]. The measurement operator for channel i is expressed as

$$M_0^i = \beta_{II}^i + \beta_{ZI}^i ZI + \beta_{IZ}^i IZ + \beta_{ZZ}^i ZZ. \quad (5.4)$$

We have three channels, measurements of state of both the qubits and their correlation. We use single qubit rotations called as tomographic pre-rotations to obtain $M_j = R_j^\dagger M_0 R_j$. For every state preparation the tomographic pre-rotations are taken from $\{\mathbb{1}, X_\pi, X_{\frac{\pi}{2}}, X_{-\frac{\pi}{2}}, Y_\pi, Y_{\frac{\pi}{2}}, Y_{-\frac{\pi}{2}}\}$. For example, when we apply the pre-rotations $T_1 = Y_{\frac{\pi}{2}}$ and $T_0 = Y_{\frac{\pi}{2}}$, the measurement operator becomes

$$M_{yy}^i = Y_{\frac{\pi}{2}}^\dagger M_0^i Y_{\frac{\pi}{2}} = \beta_{II}^i II - \beta_{IZ}^i XI - \beta_{ZI}^i IX + \beta_{ZZ}^i XX \quad (5.5)$$

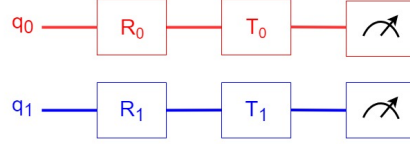


Figure 5.3: Tomography sequence for cardinal states on two qubits. Single qubit rotations R_0 and R_1 are used to prepare all 36 cardinal states. Single qubit rotations T_0 and T_1 are tomographic pre-rotations.

Upon preparing and measuring computational basis states we obtain a linear system for each channel $i = q_0, q_1, \text{corr}$, given by:

$$\langle M^i \rangle_{00} = \beta_{II}^i + \beta_{ZI}^i + \beta_{IZ}^i + \beta_{ZZ}^i, \quad (5.6)$$

$$\langle M^i \rangle_{01} = \beta_{II}^i - \beta_{ZI}^i + \beta_{IZ}^i - \beta_{ZZ}^i, \quad (5.7)$$

$$\langle M^i \rangle_{10} = \beta_{II}^i + \beta_{ZI}^i - \beta_{IZ}^i - \beta_{ZZ}^i, \quad (5.8)$$

$$\langle M^i \rangle_{11} = \beta_{II}^i - \beta_{ZI}^i - \beta_{IZ}^i + \beta_{ZZ}^i. \quad (5.9)$$

This can be written in the compact form as:

$$\vec{M} = C\vec{\beta} \quad (5.10)$$

where C is the matrix of coefficients of β terms. The next step involves removing the offset β_0^i . This done by subtracting measured value of a computational state by average of measured values for all computational states as $\beta_0^i = (\langle M_i \rangle_{00} + \langle M_i \rangle_{01} + \langle M_i \rangle_{10} + \langle M_i \rangle_{11})/4$. We then scale the measured values in each channel by the dominant β value. For example for the correlation channel we expect β_{ZZ}^{corr} to dominate both $\beta_{ZZ}^{q_0}$ and $\beta_{ZZ}^{q_1}$. So we scale measured values in the correlation channel by $M_{00}^{\text{corr}} + M_{11}^{\text{corr}} - M_{10}^{\text{corr}} - M_{01}^{\text{corr}}$. This ensures that $\beta_{ZZ}^{\text{corr}} = 1$. The next step involves measuring the noise in each channel and scaling the measured values such that the noise in each channel is the same[ref (7)]. This is done by measuring the calibration segments a few times(7 in our experiments) and taking the standard deviation.

β_{II}	β_{IZ}	β_{ZI}	β_{ZZ}
0	.9092	-5.27×10^{-3}	-0.037
0	-0.0381	2.3397	0.033
0	.189	.0945	0.678

Table 5.1: Table of β s, in the order channel q_0 , channel q_0 , channel correlation(q_0, q_1) from top to bottom.

5. EXPERIMENTAL METHODS

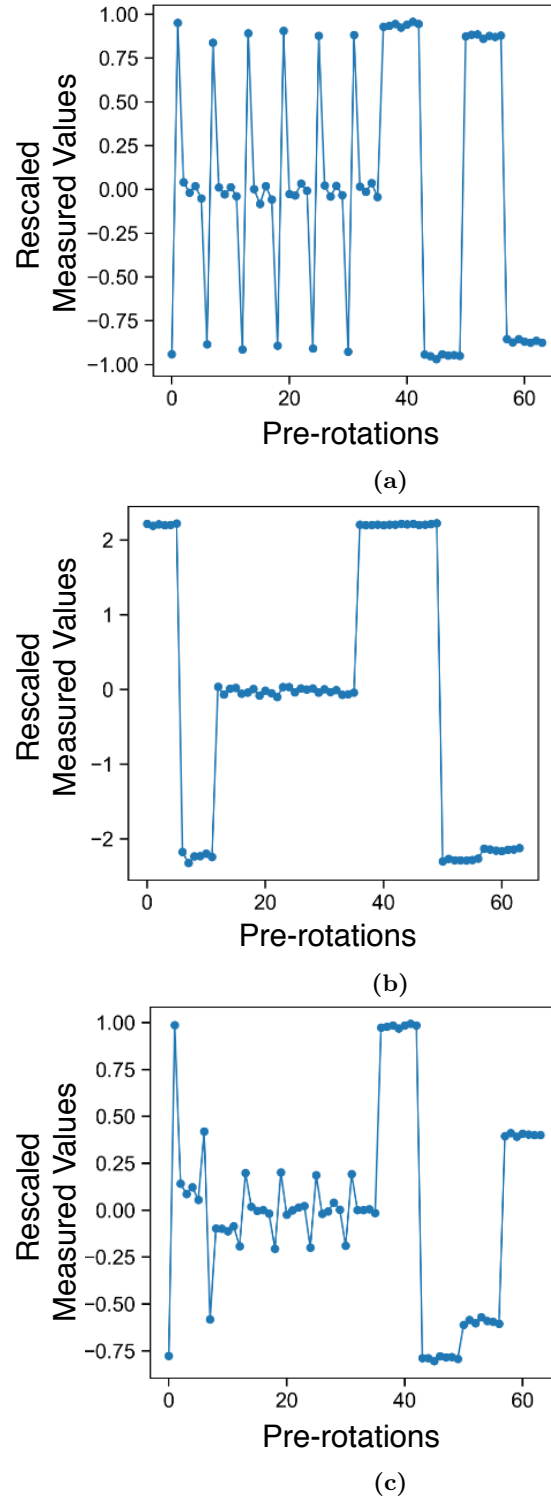


Figure 5.4: Plot of measurement values(y-axis) of each channel after removal of offsets and scaling for the state $|01\rangle$, which in our convention is $|q_1q_0\rangle$. The sequence consists of 36 pre-rotations[ref (26)] followed by 7×4 calibration measurements(x-axis). Panel (a) qubit shows processed measurement results for q_0 , which is in the excited state. (b) qubit q_1 is in the ground state and (c) correlation of q_0 and q_1 .

Having obtained the model of measurement operators, we use the measured values obtained after applying pre-rotations to estimate the density matrix[ref (7)].

$$\vec{m} = M[\rho]_P \quad (5.11)$$

Where \vec{m} is a column vector of measured values with length given by number of pre-rotations times number of channels. M is the matrix composed of β s, where each row contains entries of transformed measurement operator corresponding to a particular pre-rotation for a particular channel. The number of rows is given by number of measurement channels times number of pre-rotations and the number of columns are given by the number of basis coefficients. Clearly M is a skinny matrix (more rows than columns) and the linear system is overdetermined, i.e. we have more measurements than unknowns. We solve this system approximately by using least-squares minimization. The least-squares (approximate) solution to this system is given by

$$[\rho]_P = M^+ \vec{m} \text{ where } M^+ = M^T (MM^T)^{-1} = (M^T M)^{-1} M^T. \quad (5.12)$$

Where M^+ is the short-hand for Moore-Penrose pseudoinverse. Note that in this method we have not enforced physicality constraints like trace one and Hermiticity, so the method does not guarantee the estimated density matrix to have non-negative eigenvalues and we therefore obtain non-physical density matrices.

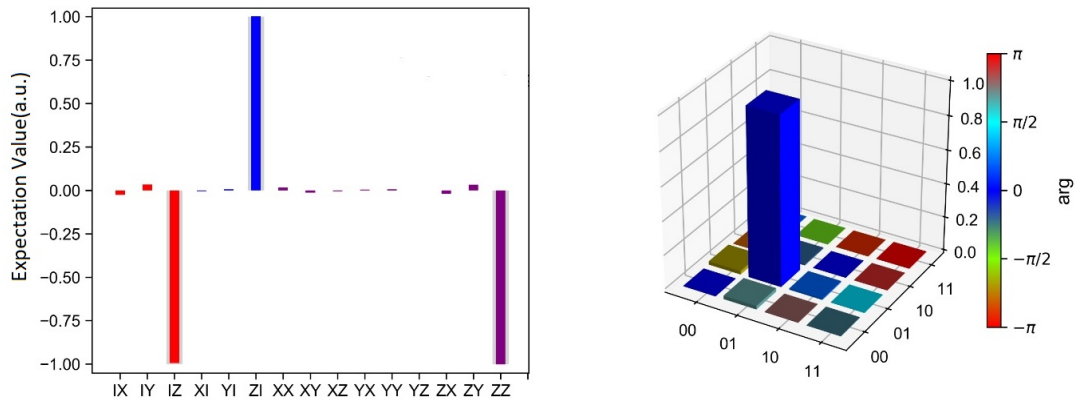


Figure 5.5: Pauli label plot and denisty matrix histogram of $|01\rangle$

It is possible to calculate only the 6 Pauli operators that occur in Hydrogen Hamiltonian of eqn 2.10, by using eight tomographic pre-rotations and calibration measurements. For a complete set of transformations of measurement operator under tomographic pre-rotations,

5. EXPERIMENTAL METHODS

please refer to [ref (7)]. The operators $\{II, IZ, ZI, ZZ\}$ require one tomographic pre-rotation each whereas the correlation terms $\{XX, YY\}$ require two pre-rotations each. We can assemble the matrix inversion problem in a similar manner as described above, leading to the eqn 5.12. This procedure is referred to as partial tomography and is essential in maintaining a polynomial scaling of the number of operations required to do a VQE as a function of qubits. This technique however results in more errors and we will not use it in the proof-of-principle experiments described in the next chapter.

5.4 Two-Qubit gates

5.4.1 Theory of Two-Qubit Gates

In Superconducting Qubits there are several ways of implementing two qubit entangling gates[ref (29),(23)]. We use a parameterized iSWAP gate in our work which generates a variable amount of entanglement in the prepared states, as required for our Ansatz. The iSWAP gate[ref (23)] results from the time-evolution of a hybridized state of two superconducting qubits under a transverse coupling. The hybridized state is formed when one of the qubits is brought into resonance with the other qubit, by using a flux pulse. The flux pulse changes the frequency of transmon qubit according to eqn 4.5. The strength of the interaction between two qubits is given by $\frac{J_1}{2\pi}$, which was characterized in section 1.6 of chapter 4.

$$J_1 = \frac{g^{(1)}g^{(2)}(\Delta_1 + \Delta_2)}{2\Delta_1\Delta_2}. \quad (5.13)$$

where $g^{(1)}, g^{(2)}$ denotes the coupling of each qubit with the bus resonator. Δ_1 and Δ_2 are the detunings of each qubit from the bus resonator. The maximum value of $\frac{J_1}{2\pi}$ occurs when the two qubits are at resonance $\Delta_1 = \Delta_2 = \Delta$ and is given by $\frac{g^{(1)}g^{(2)}}{\Delta}$ [ref (4)]. For the qubit pair D2-A $\frac{J_1}{2\pi}$ is calculated to be $20.9(\pm 0.1)$ MHz.

Under the rotating wave approximation the interaction Hamiltonian is given by[ref (23)]

$$H_{int} = \hbar J_1(|01\rangle\langle 10| + |10\rangle\langle 01|). \quad (5.14)$$

The time-evolution under this interaction is given by the two qubit unitary $U_{2q}(t)$.

$$U_{2q}(t) = \exp\left[\frac{-it}{2}(\omega_1\sigma_z^1 \otimes \mathbb{1}^2 + \omega_2\mathbb{1}^1 \otimes \sigma_z^2)\right] \times \begin{bmatrix} 1 & 0 & 0 & 0 \\ 0 & \cos(J_1 t) & -i \sin(J_1 t) & 0 \\ 0 & -i \sin(J_1 t) & \cos(J_1 t) & 0 \\ 0 & 0 & 0 & 1 \end{bmatrix}. \quad (5.15)$$

The first sub-block of the equation represents the single qubit phase that is acquired by each one of the qubits. The second sub-block corresponds to swap operation which causes states $|01\rangle$ and $|10\rangle$ to exchange populations. At time $t = \frac{\pi}{4J_1}$ the populations in both the states are equal and the two-qubit unitary represents the $\sqrt{i\text{SWAP}}$ logical operation.

The strength of coupling depends inversely on the detuning between the two qubits, the swap interaction is suppressed when qubits are far off resonance from each other($\Delta_1 \neq \Delta_2$). We apply a sudden flux pulse to one of the qubits (qubit A in the experiments described in this thesis) and bring it into an avoided crossing with the other qubit(qubit D2 in the experiments described in this thesis), for a time t. This means at time $t' = 0$, the fundamental frequency

5. EXPERIMENTAL METHODS

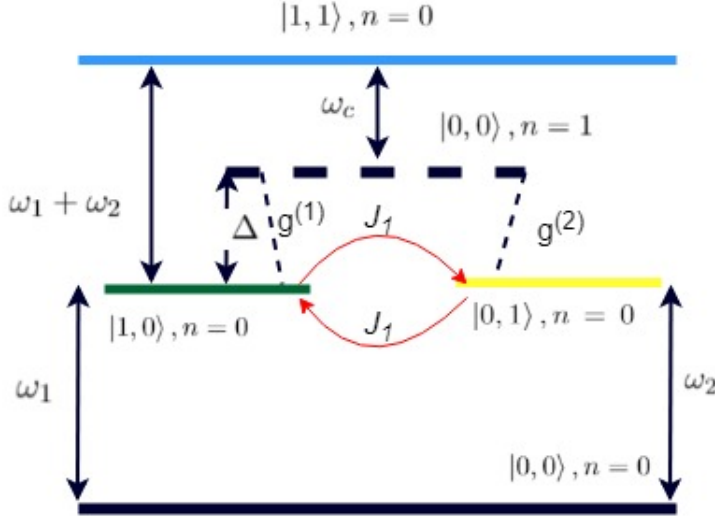


Figure 5.6: Energy level for virtual photon swap interaction. When both the qubits are detuned from the cavity(dashed black line), both the qubits dispersively shift the cavity. The excited state on the left qubit $|1, 0\rangle, n = 0$ interacts with the excited state on the right qubit $|0, 1\rangle, n = 0$ by the exchange of a virtual photon $|0, 0\rangle, n = 1$ in the cavity. In this diagram $\Delta_1 = \Delta_1 = \Delta$, corresponding to the resonance condition. Adapted from J.M. chow's thesis[ref (4)].

of the qubits are not equal i.e. $\omega_1^{01}(0) \neq \omega_2^{01}(0)$ but at time $t' = t_{rise}$ the frequencies are tuned to be equal $\omega_1^{01}(t_{rise}) = \omega_2^{01}(t_{rise})$. Then they are kept in resonance up for a time t and then brought back. If we put an excitation on the qubit being fluxed i.e. start with a state $|01\rangle$, the state after applying the flux pulse is $\cos(\theta)|01\rangle - i\sin(\theta)|10\rangle$, where $\theta = J_1 t$, apart from the single qubit phases acquired by both the qubits. When $\theta = \frac{\pi}{4}$, we produce a state of maximum concurrence, ie. a Bell state($|\Psi^\pm\rangle$), apart from single qubit phases. In the rest of the work we call this two qubit gate $iSWAP(\theta)$. The two qubit unitary generated from the swap interaction described above can be written in terms of a two-qubit entangling operation and two single-qubit unitaries.

$$U_{2q}(t) = U_{iSWAP}(\theta(t))U_{1Q}(\phi_1(t))U_{1Q}(\phi_2(t)) \quad (5.16)$$

The strength of coupling J_1 dictates the lower bound of time-duration of $iSWAP(\theta)$ gate, for any θ . The single qubit phases acquired by the qubits is a time integral of their detuning from their respective sweet-spot frequencies.

$$\phi_{ij}(t) = \int_0^t \Delta_{ij}(t') dt' \quad (5.17)$$

The next two sections describe the methods to correct for the distortions in flux pulses caused by room-temperature and cryogenic components. In sections 5.4.4 we will report the data from an experimental implementation of an iSWAP(θ) gate. This will consist of studying the expectation values of qubits that participate in the swap interaction and the phases acquired by these qubits.

5.4.2 Correction of Flux-Line Distortions

Flux pulses arriving at the qubit are distorted because they travel through several electronic components like cables and filters after being generated by the QWG. To achieve the precision in qubit frequency tuning, a calibration procedure is implemented that corrects for these distortions. In the calibration procedure we first correct the distortions caused by the room temperature components. The flux pulse generated by the QWG enters the RF-port of a bias-tee where it is combined with a current-bias. The bias-tee acts as a high pass filter which filters out the strong low frequency components of $1/f$ noise. To measure the distortions caused by bias-tee and cables we connect the output port of the bias-tee to a fast oscilloscope (RS RTO 1024, 5 GSa/s) using a cable identical to the one going in to the fridge. Following is the basic outline of the procedure that was followed:

1. Program a square pulse into the QWG, measure the response with the oscilloscope.
2. Normalize the data from the oscilloscope by the amplitude of the input square pulse, this is called the step response.
3. Fit the step response to physically motivated or heuristic models, obtain the fit parameters. The fit for the longest timescale should be applied first.
4. Obtain the inverse impulse response in terms of fit parameters.
5. The pre-distorted pulse is the convolution of square pulse in step 1 with the inverse impulse response.
6. Measure the step response of the pre-distorted pulse and repeat 2-5 until a square pulse is obtained at the output.

We used two decay models in the corrections we performed, the high-pass filter model and exponential decay. For more details on Room Temperature distortions and fit models refer to [Livio's thesis]. Given below is a table that summarizes the fit models we used and the fitting parameters.

5. EXPERIMENTAL METHODS

Model	$\tau(\mu\text{s})$	Amplitude
High-Pass Filter	40.915	None
Exponential	15.026	0.1312878
Exponential	6.408	0.990883
Exponential	3.5405	-0.07471
Exponential	1.05852	-0.01757

Table 5.2: Summary of fit parameters for Room Temperature corrections.

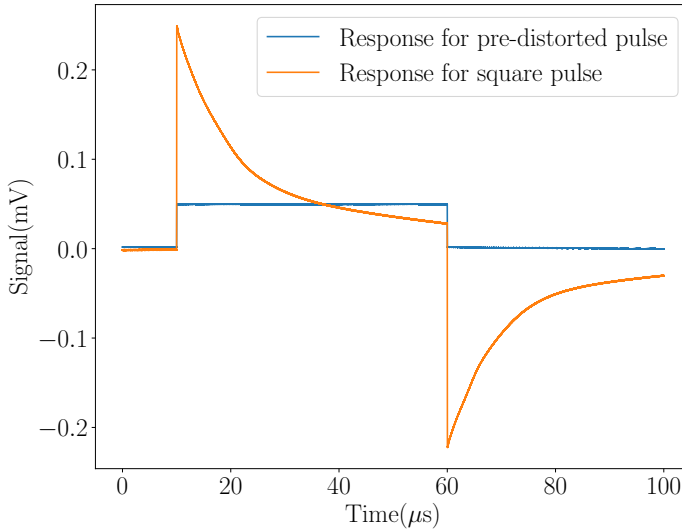


Figure 5.7: Orange curve depicts the measured output signal which has passed through all the room temperature components, for a square pulse input. Blue curve depicts the resulting signal after pre-distorting the square pulse using several models(see table). The deviation from the targetted square pulse was around 2%. The room temperature flux corrections are applied in the timescale of a typical experimental run, which in our case is 200 .

5.4.3 Cryogenic Distortions

The second step in correcting distortions involves using the qubit as cryogenic oscilloscope[ref (35)]. The pulse scheme for the cryoscope experiment is based on the Ramsey sequence. Two $X_{\frac{\pi}{2}}$ pulses are played with a fixed delay τ in between them. During this time τ a flux pulse of variable length(t_p) is played. The measurement is repeated for different flux pulse lengths, to measure the qubit phase ϕ as a function of t_p . The phase acquired by the qubit between the two $\frac{\pi}{2}$ pulses is given by eqn 5.17. The detuning is a function of the amplitude of the flux pulse, $\Delta_{01}(t) = \Delta_{01}(V(t))$. Assuming a small distortion $\delta V(t)$ from the targetted pulse shape $\tilde{V}(t)$, it can be shown using Taylor expansion that[ref (6)]

$$\frac{d}{dt_p} \phi = \Delta_{01}(\tilde{V}(t) + \delta V(t)) = \Delta_{01}(t_p), \quad (5.18)$$

which gives the instantaneous detuning of the qubit at time t_p . From the knowledge of the detuning we can calculate the flux pulse shape experienced by the qubit using

$$V = \frac{V_{\Phi_0}}{\pi} \arccos \left(\left(\frac{\hbar\omega_{01} + E_C}{\hbar\omega_{01,max} + E_C} \right)^2 \right) + V_0 \quad (5.19)$$

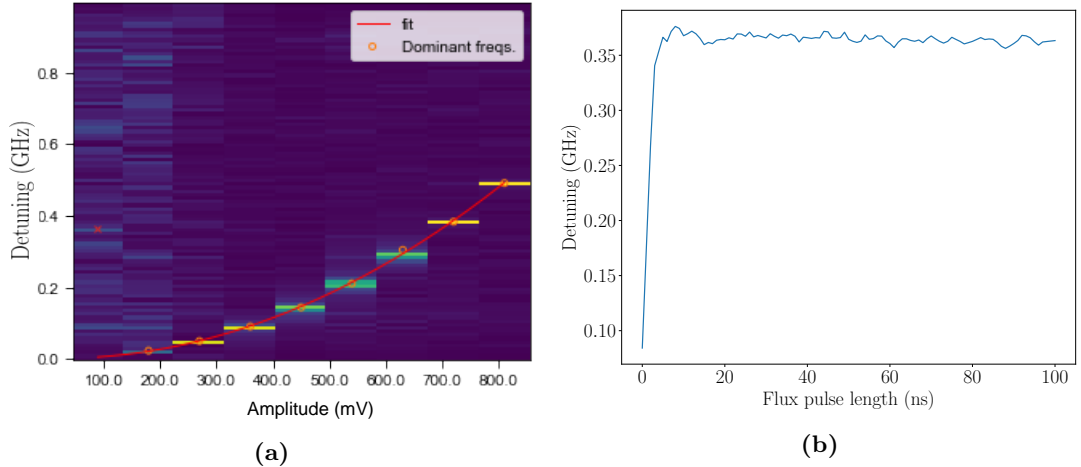


Figure 5.8: Amplitude calibration arc (a) obtained through a cryoscope experiment repeated for different flux pulse amplitudes. The detuning of the qubit increases with increasing amplitude. Distortions in flux pulses lead to a smearing of peaks. The right panel shows instantaneous detuning as a function of flux pulse length for an amplitude of 700 mV, which will be used to bring the qubit being fluxed(A) into an avoided crossing with the other qubit (D2). Data in (b) was obtained after correcting for bounces, therefore corresponds to Fig 5.9 (b). The detuning reported here is 500 MHz(QWG samples at 1ns) less than the actual detuning because we are at the second Nyquist order.

5. EXPERIMENTAL METHODS

Where V_{Φ_0} is the voltage equivalent of flux quantum through the SQUID loop of the transmon qubit, V is scaled in a similar manner as $V = (V - V_0)\frac{\Phi_0}{V_{\Phi_0}}$. This formula assumes a symmetric transmon. Furthermore, we do not measure the phase through two $X_{\pi/2}$ pulses directly, instead we measure the probability of the qubit being in the excited state($p_{|1\rangle}$), as described in the section 4.2.3. $p_{|1\rangle}$ is given by $(1 + \cos(\phi))/2$. If we replace the second pulse by an $Y_{\pi/2}$ pulse, we can reconstruct the phase by using

$$\phi = \arctan\left(\frac{2p_{|1\rangle}^{\sin} - 1}{2p_{|1\rangle}^{\sin} - 1}\right) \quad (5.20)$$

In Fig 5.8(a) we present the amplitude calibration arc which gives the detuning as a function of amplitude of the square pulse. This is obtained by repeating the procedure to find $\sin(\phi(t_p))$ for different square pulse amplitudes and computing the FFT to obtain the dominant frequencies. The phase ϕ calculated from the equation 5.20 needs to unwrapped before the calculation of the derivative to determine the detuning. For a detailed overview of the steps please refer to the Masters thesis of Livio Ciorciaro[ref (6)].

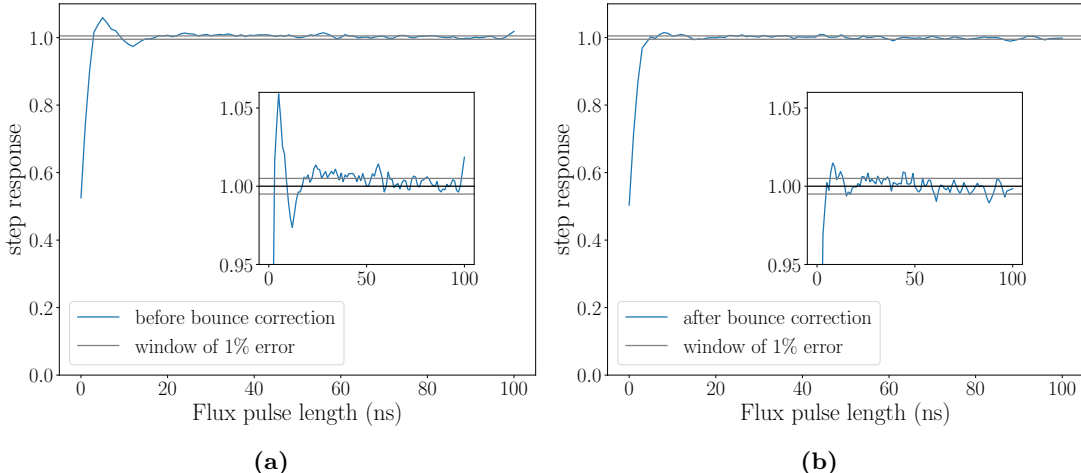


Figure 5.9: Cryogenic step response measured using a cryoscope before (a) and after applying two bounce corrections at 15ns and 8ns with amplitudes

In the figure 5.9(a) we present the normalized step response calculated from the instantaneous detuning with only room temperature corrections applied. At short timescales we find transmission line bounces or echoes, which result from steps in impedance. The step response of a bounce effect is given by

$$h(t) = \Theta(t) + \sum_i A_i \times \Theta(t - t_i). \quad (5.21)$$

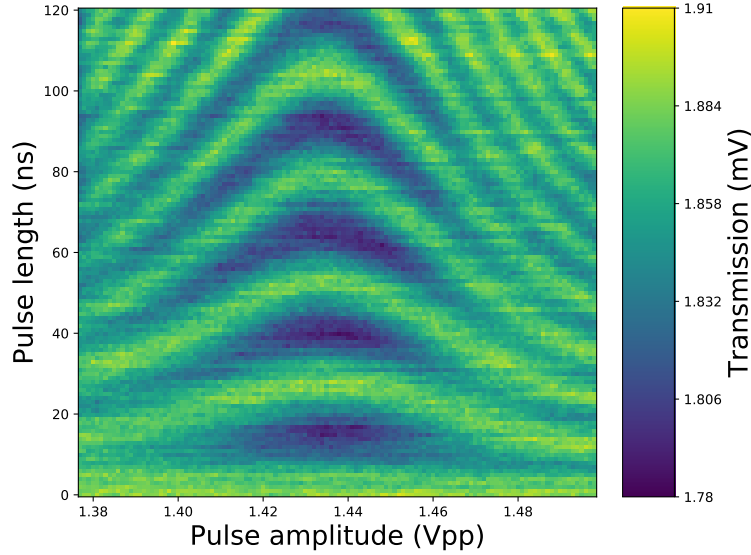


Figure 5.10: Measurement of coherent oscillations(the chevron pattern) at the $|01\rangle \leftrightarrow |10\rangle$ avoided crossing after correcting for distortions. The central slice of the chevron represents the amplitude(of the flux pulse) at which qubit A comes into resonance with qubit D2 and hence the iSWAP gate is implemented as a vertical cut of this plot. The oscillations along y-axis represent exchange in populations between the two qubits.

The model parameters to be calibrated are $\{A_i, t_i\}$. The parameters of the bounces in our system were found to be $(15\text{ ns}, 0.02)$ and $(8\text{ ns}, -0.045)$. Figure 5.9(b) gives the step reponse measured after correcting for the bounce effect. We see that we obtain a correction to within 1% beyond 15 ns, even the small bounce in the first 15ns is within 2.5%.

We conclude the section on distortion correction by reporting the chevron pattern (Fig 5.10) obtained after distortion corrections. The experiment consists of putting an excitation (Y_π) on to a qubit, then applying flux pulses of varying lengths and amplitudes on to the same qubit. By reading out the qubit we obtain populations that will oscillate with the length of the flux pulse. This gives rise to the iSWAP interaction, which is implemented as the central vertical slice of the chevron pattern. If there are distortions in the flux pulse this will lead to a smearing of the chevron pattern. The pulse scheme for obtaining the chevron pattern infact has all the elements needed for the particle number conserving ansatz, except the phase correction and sampling of all Pauli operators and phase correction gate.

5. EXPERIMENTAL METHODS

5.4.4 Implementation of iSWAP Gate For VQE experiments

After correcting for the distortions in flux pulses, we will now describe the evolution of qubits that participate in the iSWAP gate. We start by putting one excitation in the qubit A, the resulting state is given by $|D2, A\rangle = |01\rangle$. We then apply flux pulses of varying lengths to qubit A. The amplitude of the flux pulse is taken from the central slice of chevron pattern, which corresponds to the qubits being in resonance. We then apply single-qubit tomographic pre-rotations on both the qubits to perform quantum state tomography as described in section 5.3, to extract expectation values of relevant operators. The relevant operators are $\{IZ, ZI, ZZ, XX, YY\}$, they are sufficient to demonstrate the population exchange and entanglement. The state after the iswap becomes

$$|\psi_{iSWAP}\rangle = \cos(\theta) |01\rangle - ie^{i(\phi_A - \phi_{D2})} \sin(\theta) |10\rangle. \quad (5.22)$$

Here θ depends on the length of the flux pulse. The state in general should be represented by a density matrix, but this expression suffices to garner intuition for the evolution of expectation values as a function of flux pulse length. For this state we give the expectation values a function of θ of relevant operators:

$$\begin{aligned} \langle IZ \rangle &= -\cos(2\theta), \langle ZI \rangle = \cos(2\theta), \langle ZZ \rangle = -1, \\ \langle XX \rangle &= \sin(2\theta) \sin(\phi_A - \phi_{D2}), \langle YY \rangle = \sin(2\theta) \sin(\phi_A - \phi_{D2}) \end{aligned} \quad (5.23)$$

The phase acquired by the qubit A changes rapidly, therefore to isolate the θ dependence we will use the operators $\{XY, YX\}$ to eliminate it.

$$\begin{aligned} \langle XY \rangle &= \sin(2\theta) \cos(\phi_A - \phi_{D2}), \langle YX \rangle = \sin(2\theta) \cos(\phi_A - \phi_{D2}) \\ \sqrt{\langle XY \rangle^2 + \langle XX \rangle^2} &= |\sin(2\theta)|, \sqrt{\langle YX \rangle^2 + \langle YY \rangle^2} = |\sin(2\theta)| \end{aligned} \quad (5.24)$$

In Fig 5.11 we see oscillations in the expectation values as expected. The operators that govern population exchange IZ and ZI are 180 degree out of phase as expected from eqn 5.22. Parity stays close to -1, in Fig 5.11. The mean value of parity is -0.96 and the standard deviation is 0.014. The oscillations for mean squared operators completely overlap, with a period half that of oscillations in populations. The maxima of this oscillation occurs when the length of the flux pulse is 8ns. This is the \sqrt{iSWAP} point. We know from the theory of the iSWAP gate that this length should be given by $\frac{\pi}{4J_1} = 5.9$ ns. This discrepancy can be explained by the

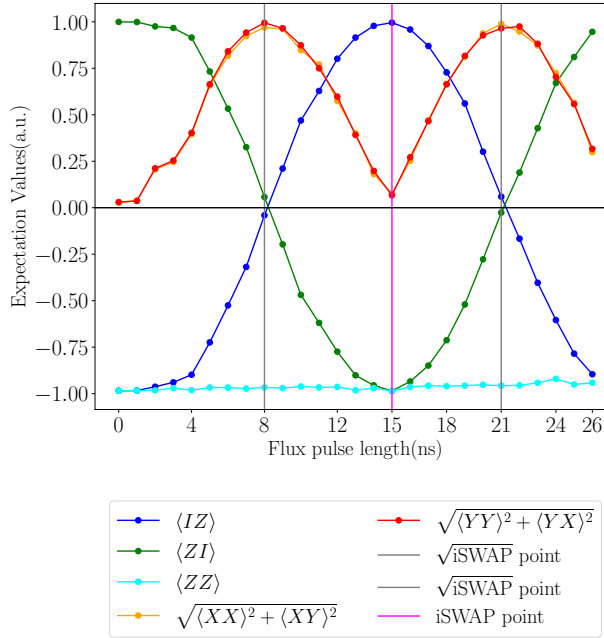


Figure 5.11: Expectation Values of Pauli operators $\{IZ, ZI, ZZ, XX, XY, YX, YY\}$ as a function of flux pulse length. The operator sets $\{XX, XY\}$ (orange dots) and $\{YY, YX\}$ (red dots) are clubbed together to correct for the phase acquired by the qubit being fluxed. Grey vertical lines denote the \sqrt{iSWAP} point, where maximum concurrence is reached in the prepared state. Magenta vertical line represents the iSWAP point, where the population exchange is completed(red and green dots).

offset that is seen in the oscillations in Fig 5.11. We then move onto to study the phase that is acquired by qubit being fluxed(A) and the qubit not being fluxed(D2). To this we prepare the state $|D2, A\rangle = |-i, 0\rangle$, by applying a $X_{\pi/2}$ rotation on the qubit D2. We then apply flux pulses of varying lengths on qubit A. This is followed by tomographic pre-rotations. We use the obtained expectation values to construct a density matrix. From the phase of the coherence terms we can obtain information about the phases acquired by both the qubits. This can be seen by writing down the state after the application of flux pulse as follows

$$|\psi\rangle_{after} = \frac{|00\rangle + e^{i\phi_A} \sin(\theta) |01\rangle - ie^{i\phi_{D2}} \cos(\theta) |10\rangle}{\sqrt{2}}. \quad (5.25)$$

Where θ depends on the length of the flux pulse. From here we immediately see the proposition made above. The phase of the coherence term $\langle 01| \rho |00\rangle$ is the phase acquired by the qubit A ϕ_A , which is being fluxed. Also, to compute the phase acquired by the qubit D2 (not being fluxed) ϕ_{D2} , we simply need to look at the phase of the coherence $\langle 10| \hat{\rho} |00\rangle$.

We report the measurement of ϕ_A by using this technique in Fig 5.12. The qubit A is highly

5. EXPERIMENTAL METHODS

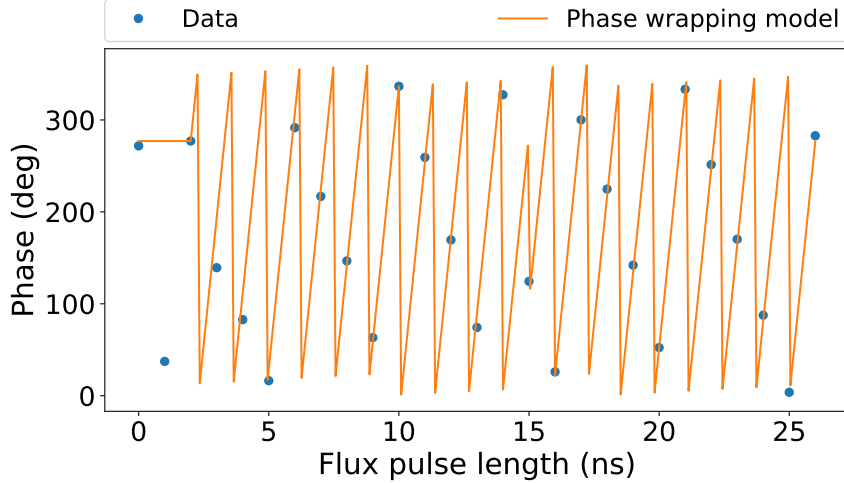


Figure 5.12: Phase acquired by the qubit being fluxed(A). The rapid oscillations are due to the large detuning A from its sweetspot. The oscillations start at 3ns, corresponding to the rise time of the flux pulse and experience a 180 degree jump at 15 ns(iSWAP point).

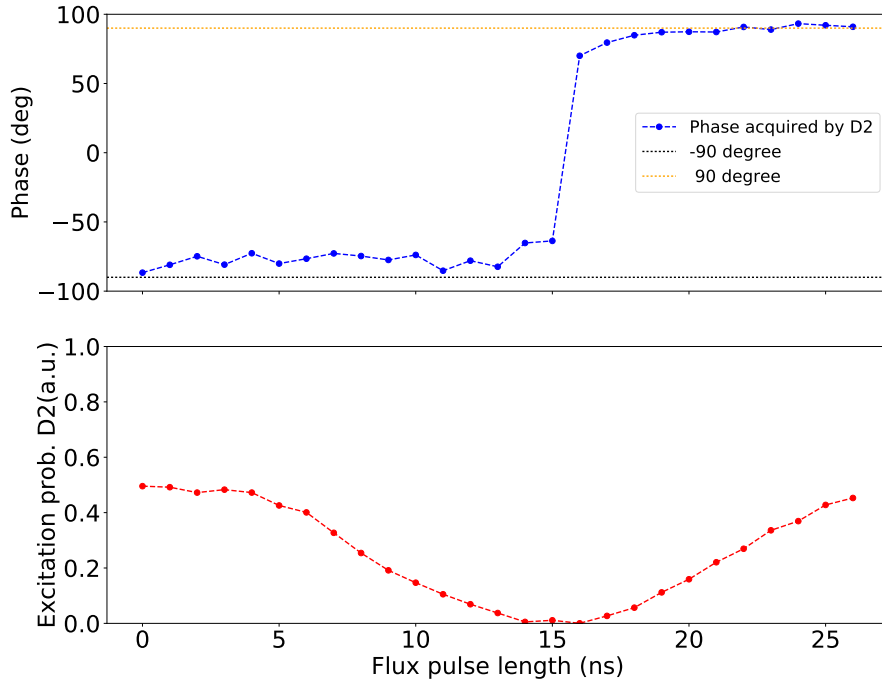


Figure 5.13: Top panel shows phase acquired by the qubit not being fluxed(D2) as a function of flux-pulse length. Also shown below is the excitation probability of the same qubit. Since the qubit starts in the state $| -i \rangle$, the excitation probability $\langle Z \rangle = \frac{1}{2}$. After completely exchanging the population(at the iSWAP point), the state of the qubit is $| 0 \rangle$. At the iSWAP point we get a 180 degree phase jump, because the coherence term acquires a factor of -1.

detuned from it's sweet-spot frequency, giving rise to fast oscillations in phase. This data will be used to correct for the phase of iSWAP in post processing when reconstructing landscapes (see Fig 6.2). In Fig 5.13 we plot the phase ϕ_{D2} , which is not being fluxed, along with the excitation probability of the qubit D2. From equation 5.12 it is clear that the qubit starts with the state $\frac{|0\rangle + |1\rangle}{\sqrt{2}}$, giving the excitation probability of $\frac{1}{2}$. As the full iSWAP point is reached ($\theta = \frac{\pi}{2}$), the state of the qubit becomes $|0\rangle$. At this point a phase jump of 180 degree occurs because cosine changes sign in the second quadrant. ϕ_{D2} should take values -90 degrees and 90 degrees, as it should not acquire any phase, because it is not being fluxed. However, we see that a phase of 15 degrees is acquired as the flux pulse length increases. This could be because we are not exactly at resonance. This data was taken with only a 1000 averages, so the sampling noise is about 3 percent. A better study is needed to make clarifications on this dataset. For our VQE experiment we will extract the phase data for qubit D2 and apply, this as real-time sideband correction on our tomographic pre-rotations, thus compensating for this phase.

We finally prepare the Bell-state $\frac{|01\rangle + |10\rangle}{\sqrt{2}}$ by using a flux pulse of length 8ns, while correcting for the phase of qubit D2 in real time by using sideband correction. We observe a fidelity of 95.5 %to the target Bell-state. We report a density matrix histogram in Fig 5.14 right panel obtained by Least-Squares tomography. The phase of the coherence terms is encoded in the color of the histogram. In fig 5.14 left panel, we report a Pauli label plot, which consists of the expectation values of 15 two-qubit Pauli operators. We see a parity($\langle ZZ \rangle$) of close to -1, as expected for a the prepared Bell state. We also see two-qubit correlations($\langle XX \rangle$, $\langle YY \rangle$) of close to +1, as expected.

For the correct implementation of $i\text{SWAP}(\theta)$ gate it is essential that both the sources providing LO for single qubit gates are phase locked. If this is not done it will lead to the averaging out of coherence terms in the density matrix as they will acquire different phases in each realization of the experiment. We achieve the phase locking by rounding off the frequencies of both the sources to 5kHz, thus both sources have a period of 200. We set the repetition time of experiment to be the same.

In conclusion we have demonstrated all the experimental methods necessary to implement the Variational Quantum Eigensolver experiment with two qubits. One of the limitations of our experimental tuneup is our readout fidelities, which are around 90 percent for both the qubits. However, since we will perform a tomography with an overcomplete set of rotations(36 pre-rotations), we should only be limited by sampling noise. The readout fidelities will be

5. EXPERIMENTAL METHODS

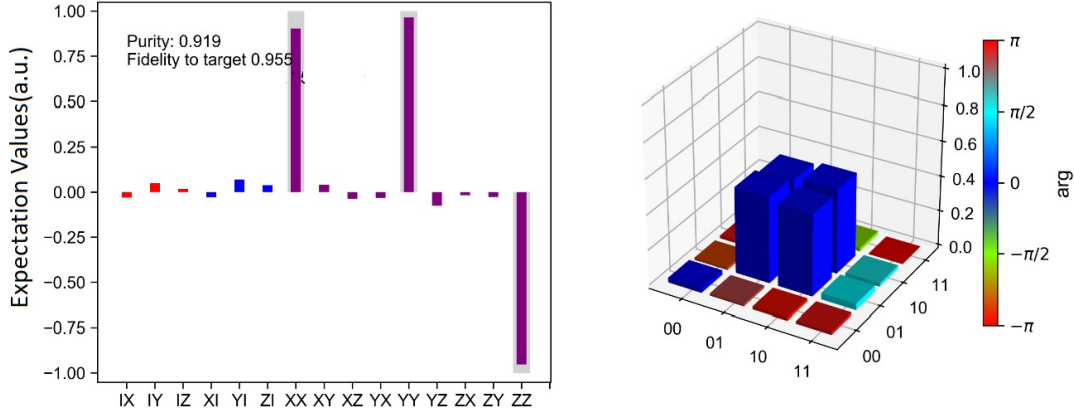


Figure 5.14: Pauli label plot(left) and denisty matrix histogram(right) of the Bell-State $|\Psi^+\rangle = \frac{1}{\sqrt{4}}(|01\rangle + |10\rangle)$ obtained through Least-Squares Tomography. The reported fidelity is obtained by contracting a vector of all pauli terms with a vector of pauli labels for the ideal Bell state. A maximum likelihood tomography of the same data gave a fidelity of 94.8%

improved in the later iterations of the experiment. In the next chapter we will demonstrate the procedure that implements the VQE algorithm.

6

Results

6.1 Variational quantum simulation without error mitigation

We use the particle number conserving circuit of chapter 2 in the VQE experiments described in this chapter. As explained before, this allows us to use the ZZ symmetry(eqn 2.11) in the Hydrogen Hamiltonian of eqn 2.10 to compensate for T_1 error. We implement the T_1 mitigation by rescaling expectation values in post processing.

The particle number conserving circuit has two control parameters which we denote by θ and ϕ . They correspond to the control parameters length of the flux pulse and the single sideband phase of the microwave pulse, applied on the qubit being fluxed. The dependence of θ on the length of the flux pulse governs the amount of entanglement in the prepared ground state. The length of flux pulse can be controlled with 1 ns resolution, giving rise to 6.14 degree resolution in θ . The phase correction gate Z_ϕ decides the phase of $|10\rangle$ state with respect to $|01\rangle$. The VQE experiments presented in this thesis do not use an optimization routine. Instead, we prepare a set of states $\{\psi(\theta_i, \phi_j)\}$ on a two-dimensional grid defined by $\{\theta_i, \phi_j\}_{i,j=1,1}^{n,m}$. We then find the ground states corresponding to each bond length in post processing. The steps taken will be explained in detail in this section. The prepared states are of the form $\cos(\theta_i)|01\rangle + \sin(\theta_i)\exp\{i\phi_j\}|10\rangle$. The state preparation circuit also contains one single-qubit gate on each qubit, to change basis for quantum state tomography. Each of these single qubit gates are taken from the set $\{\mathbb{1}, X_\pi, X_{-\frac{\pi}{2}}, X_{\frac{\pi}{2}}, Y_\pi, Y_{-\frac{\pi}{2}}\}$, given us a total of $6^2 = 36$ combinations. For every θ_i and ϕ_j we do 36+28 experiments, each with 10,000 averages, where 28 refers to 7×4 measurements of calibration points. The measured values are used to do quantum state tomography as described in section 5.6. In figure 6.1 we plot the

6. RESULTS

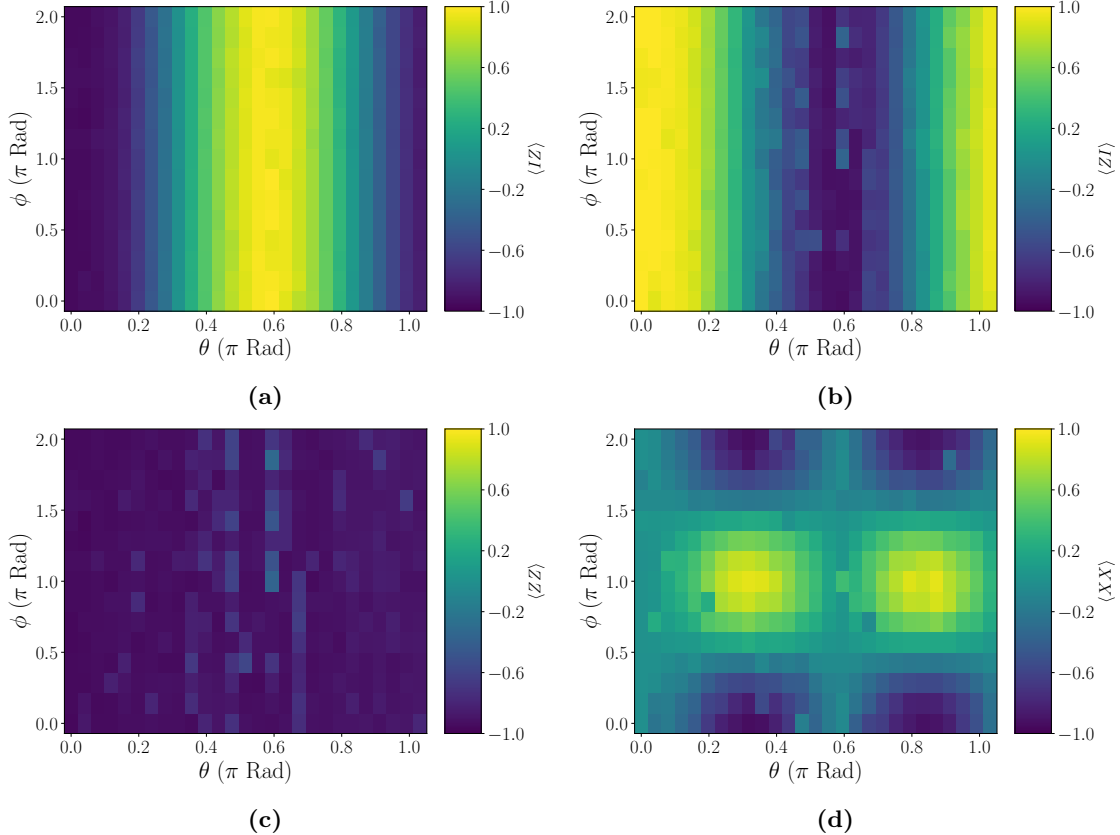


Figure 6.1: Expectation values of Pauli terms as a function of θ (angle of iSWAP) and ϕ (phase correction gate). (a) $\langle IZ \rangle$, (b) $\langle ZI \rangle$, (c) $\langle ZZ \rangle$ and (d) $\langle XX \rangle$. In the phase convention of this plot singlet bell states are formed at $\phi = 0$ and 2π .

expectation values computed from tomography (color scale) as a function of θ (x-axis) and ϕ (y-axis). In Fig 6.1 (a) the expectation value $\langle IZ \rangle_{\psi(\theta,\phi)}$ shows an oscillation along the x-axis. This is consistent with the fact that at $\theta = 0$ we have the state $|01\rangle\langle 01|ZI|01\rangle = 1$, at $\theta = \frac{\pi}{2}$ we have the state $|10\rangle\langle 10|IZ|10\rangle = -1$, corresponding to a full iSWAP and at $\theta = \pi$ we arrive at $|01\rangle$ again. The oscillation in $\langle ZI \rangle$ (Fig 6.1 (b)) is 180 degree out phase wrt $\langle IZ \rangle$ (Fig 6.1 (a)). The parity of the states $\langle ZZ \rangle$ is plotted in the Fig 6.1 (c), it is close to -1, for all the prepared states. Fig 6.1 (d) shows the expectation value $\langle XX \rangle$. In plot of $\langle XX \rangle$ we can locate two different bell states, corresponding to $\langle XX \rangle = 1, -1$. The extremeum -1 occurs at $\langle XX \rangle(\theta = \frac{\pi}{4} + l\frac{\pi}{2}, \phi = 2k\pi)$ correspond to the Bell state $|\Psi^-\rangle = \frac{|01\rangle - |10\rangle}{4}$, where $l = 0, 1$ and $k = 0, 1$ are non-negative integers. Similarly the Bell state $|\Psi^+\rangle = \frac{|01\rangle + |10\rangle}{4}$ is formed at $\theta = \pi/4, \phi = \pi$ and $\theta = 3\pi/4, \phi = \pi$. The solutions to the hydrogen Hamiltonian at large

6.1 Variational quantum simulation without error mitigation

bond lengths look like singlet Bell states.

Next, we map the expectation values to energies at different bond lengths. To this end we use the mapping pre-factors g_i s of eqn 2.10. Since we have a different set of g_i for every bond length R , we get different energy landscapes for every R . We use a total of 54 bond lengths. In fig 6.2 we plot the energy landscapes obtained experimentally at three different bond lengths alongside the energy landscapes obtained through simulation. To simulate the energy landscape we use quantumsim. We use the same circuit length as used in the experiments and use the T_1 and T_2 measured on the qubits. The raw energy landscapes obtained from an experiment have their phase scrambled, due to the fact that qubit A acquires phase during the flux pulse. The landscapes are corrected using the data of Fig. 5.12. We assert that this correction is only essential to math the experimentally obtained and simulation landscapes, not to extract the energies.

We then move onto extracting the ground state energies for all bond lengths(54 points). This is done by simply constructing all landscapes and finding their minimas. Fig 6.3 (a) shows the dissociation curve (dark blue) obtained by following the procedure detailed above. We plot the dissociation curve obtained through the simulation described above as well (in black). This curve summarizes the results of variational quantum simulation of hydrogen molecule. We call this the bare VQE experiment. The experimentally estimated ground state energies have more error than the simulation. We know from the Variational principle that errors in prepared ground state raise the energy, this is confirmed from the reported energy minimas. The value of energy minimas found using the experiment are higher. An advantage of our technique is that we do not have to repeat the state preparation for every bond length as would have been the case if we used an optimizer. Mapping can be done entirely in post-processing. To compute the error in energy estimation we subtract the experimentally obtained ground state energies from energies obtained through numerical diagonalization of hydrogen hamiltonian of eqn 2.10. The error in energy estimation (Fig 6.3 (b)) shows that we are about two order of magnitudes away from chemical accuracy. To study the properties of ground states in detail we plot the expectation values of Pauli terms occurring in the Hamiltonian as a function of bond length in Fig 6.4. Both the experimentally obtained and simulated expectation values of parity deviate from the true value of -1.

The error in ground state energy estimation shows a wave like pattern(Fig 6.3 (b)). This is because we have a high discretization in the angle of the iSWAP. We use the same θ to compute the solution of multiple points on the dissociation curve. As a result the error is lower at the

6. RESULTS

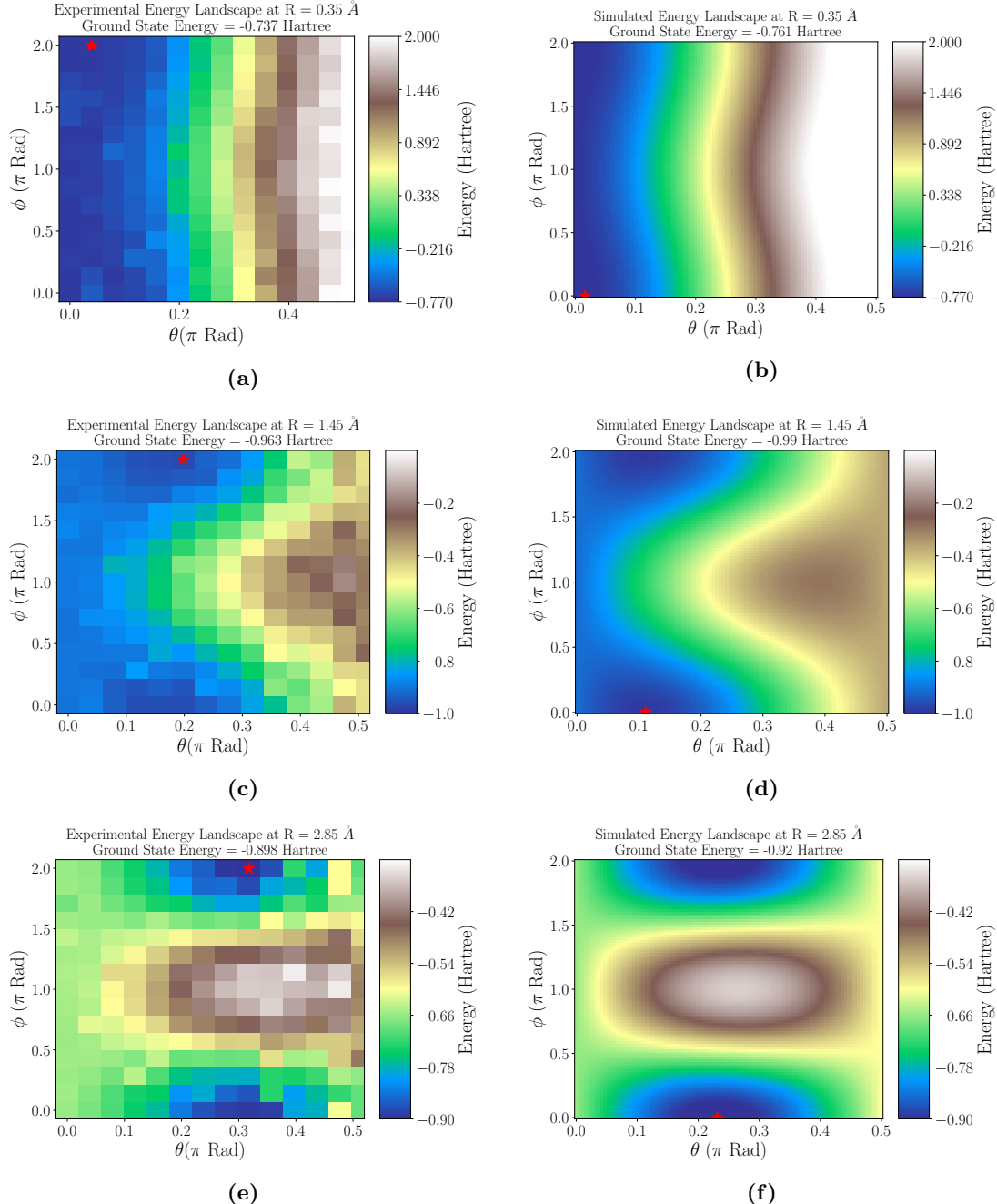


Figure 6.2: Energy landscapes obtained after mapping the expectation values obtained through tomography in (a), (c) and (d). Energy landscapes obtained through a quantum simulation of the same circuit in (b), (d) and (e). The simulated landscapes have a much smaller discretization. The minima of the landscapes are shown as red stars. For the simulation data all minimas lie on the segment $\phi = 0$, but for the experimental data they all lie on the axis $\phi = 2\pi$. The simulations are periodic, with a period of 2π along y-axis.

6.1 Variational quantum simulation without error mitigation

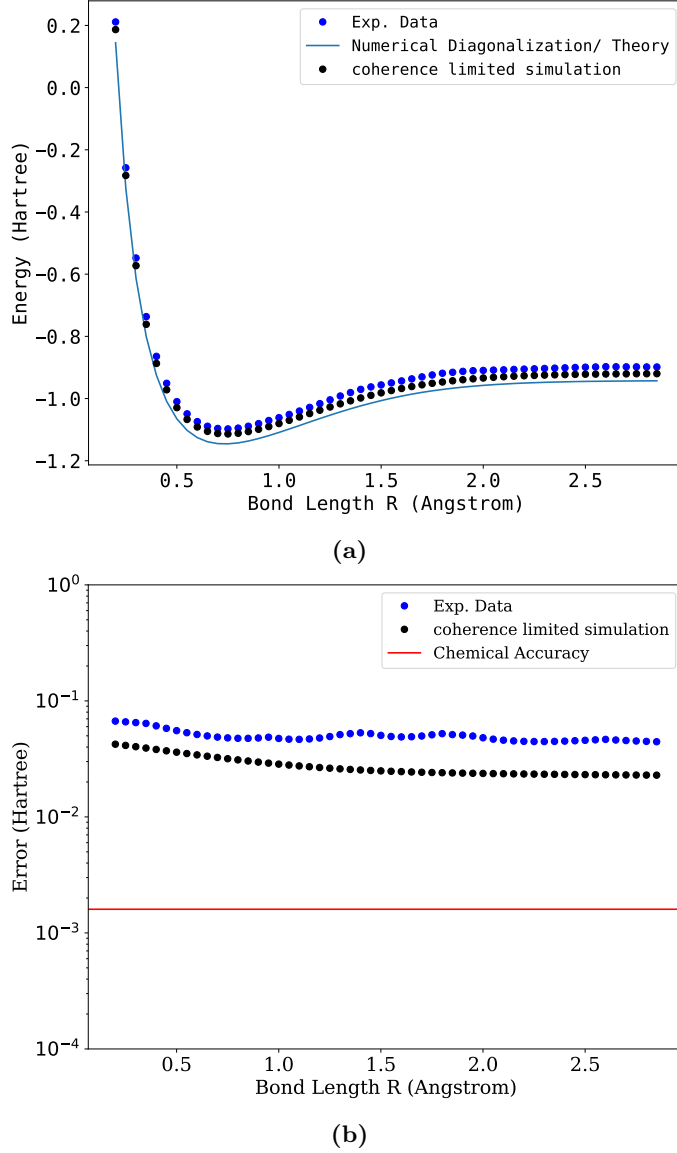


Figure 6.3: Results from a VQE experiment. (a) Plot of experimentally computed ground state energy (dark blue). Also shown are ground state energies obtained via numerical diagonalization (light blue) and simulation with a basic error model.(b) Plot of the error in the energy estimation.

point which is closest to the true solution in θ , and then it rises as bond length increases and we go away from the true solution. The error finally falls as we come closer to the next true solution and a second minima occurs. We conclude from this plot that we are discretization limited. As a first step towards a state-of-the art experiment we should use a control knob which gives us a lower discretization in θ . To this end we can use the amplitude of the flux

6. RESULTS

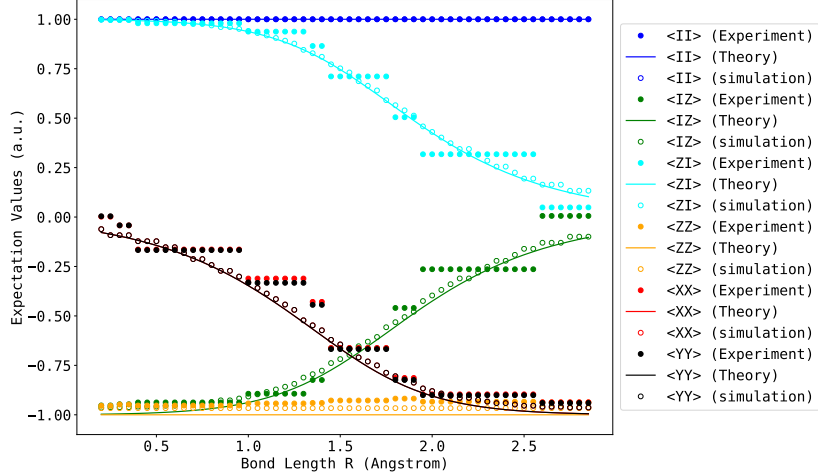


Figure 6.4: Experimentally obtained expectation values of pauli terms(filled circles) occurring in the hydrogen Hamiltonian of eqn 2.10. Also shown are expectation values calculated via numerical diagonalization(continuous lines) and via coherence limited simulation(empty circles).

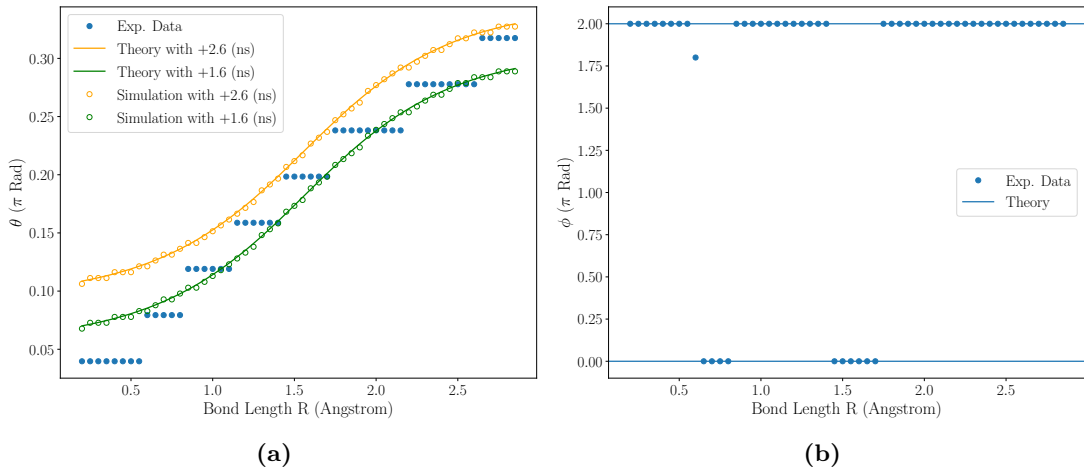


Figure 6.5: Control parameters as function of bond length. Angle of iSWAP in (a) as a function of bond length obtained from experiment (blue filled circles). There are only 8 unique values of theta as the flux pulse takes the values from $t = 0$ ns to 7 ns in steps of 1 ns. The disagreement between experimental data and simulation/theory is likely due to a low pass effect which results in qubits to not exchange any populations between states $|01\rangle$ and $|10\rangle$ when the flux pulse is small. For comparison theory and simulation results with two different offsets with 1.6 ns and 2.6 ns are also shown. The values for predicted ϕ are in well agreement with the theory as both values 0 and 2π produce the same energy in theory.

6.1 Variational quantum simulation without error mitigation

pulse instead of it's length to control the population exchange. In the experiment reported above a large buffer was used between the flux pulse and tomographic pre-rotations to avoid the tail of the flux pulse interfering with pre-rotations. In the experiment the circuit length was 180 ns (without the measurement pulse), whereas our targetted circuit length is under 50ns. We have taken this into account in our simulations reported in the plot as a waiting gate. The obtained error is an order of magnitude higher than the simulations reported in chapter 3, this can be attributed to a large extent to the buffers used in our circuit. Therefore, the error in ground state energy estimation in the bare VQE experiment could be further decreased even with this discretization in θ .

Our strategy for finding ground states experimentally can be summarized as follows:

1. **Prepare states** $|\psi(\theta_i, \phi_j)\rangle$ on a grid of (θ_i, ϕ_j) .
2. **Do quantum state tomography** after every state preparation and calculate all the two qubit pauli terms.
3. **Map Pauli terms** at every θ and ϕ to energy in post processing. This gives rise to landscapes of energy, $E(\theta, \phi)$. There exists a unique landscape at every bond length with a discernable minimum.
4. **Find the minima of landscape** $E(\theta, \phi)$ for all bond lengths.

6. RESULTS

6.2 T_1 mitigation by rescaling

We can apply the T_1 mitigation by expectation value rescaling technique from the data obtained in a bare VQE experiment in post processing. This is done by first rescaling the expectation values obtained through tomography by using the equations 3.15 and 3.16, given in chapter 3. We then follow the steps 3 and 4 described in the last section. We also simulate the experiment by following the same procedure as before. T_1 mitigation rescales the expectation values of pauli terms such that a parity of -1 is enforced. The expectation values $\langle \cdot \rangle$ and $\langle \cdot \rangle$ are enforced to be equal by this technique, as can be seen in Fig 6.6 (a), red and black curves completely overlap.

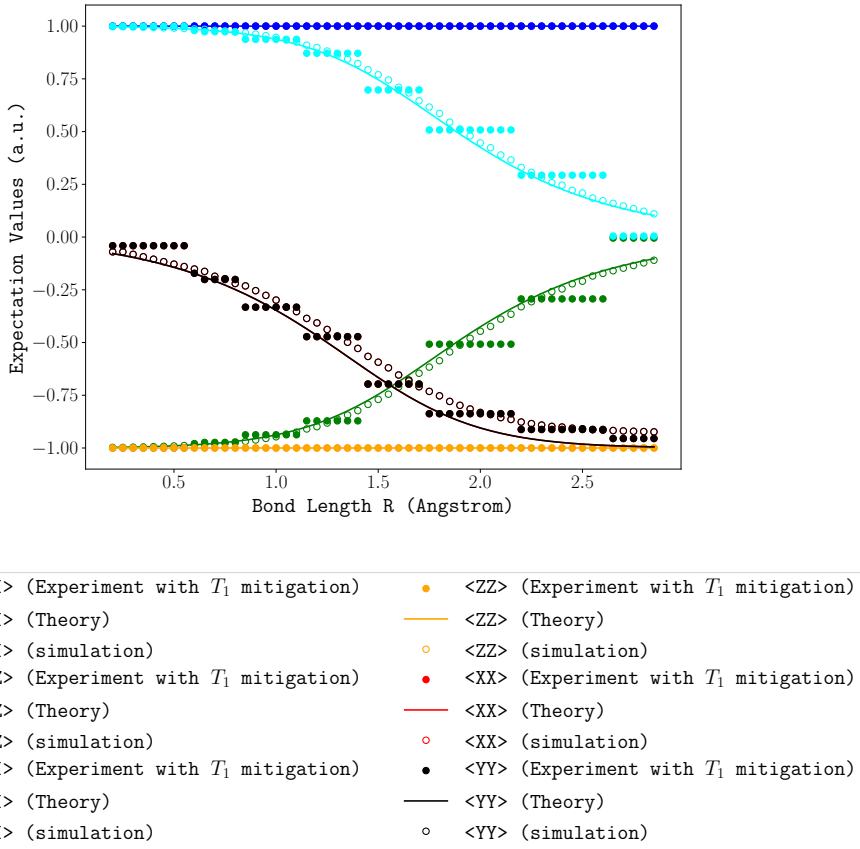


Figure 6.6: Results from a VQE experiment with T_1 mitigation. (a) Plot of expectation values as a function of bond length for three sets of data; experiment, theory and simulation. The parity, $\langle ZZ \rangle$ is equal to -1 for theory, experiment and simulation. $\langle XX \rangle = \langle YY \rangle$ are equal for all three sets of data. This signals a successful enforcement of parity conservation.

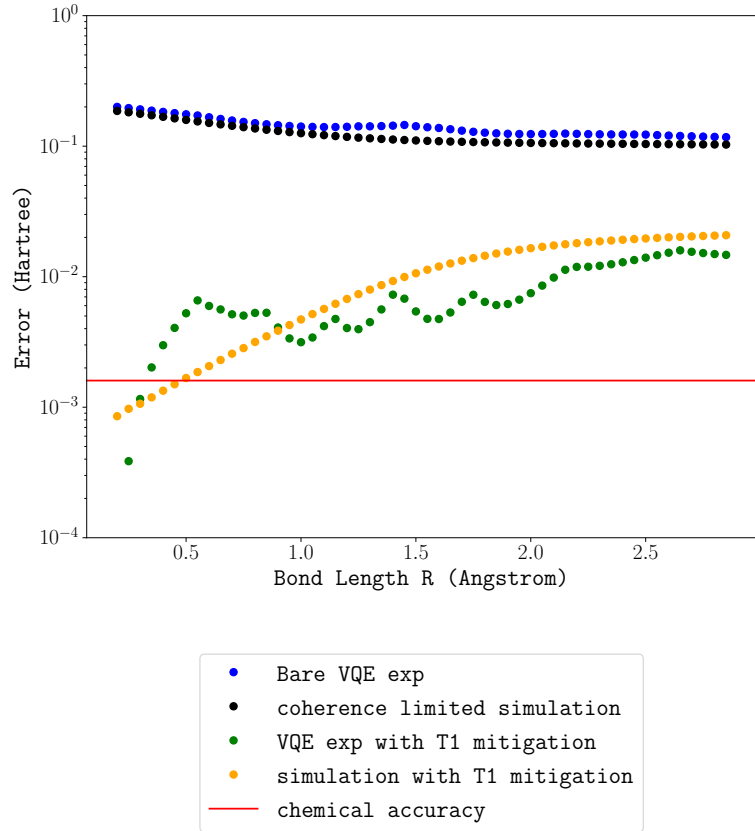


Figure 6.7: Error in Energy estimate. T_1 mitigation results in one to two orders of magnitude in error reduction. After error mitigation we see an increasing trend in error this is because we still have errors caused by finite T_2 , these become more prominent as concurrence becomes higher.

The experiment from which we report the dataset in Fig 6.6 and Fig 6.7 had a very high buffer due to a human error. Therefore, the error in bare VQE experiment (Fig 6.7 dark blue dots) on which T_1 mitigation is done has a higher error than the bare VQE experiment reported in the previous section. The experimentally obtained Bare VQE curve is very close to the simulation with a basic error model, this can be explained by higher errors due to qubit relaxation and dephasing. The simulation of T_1 mitigation technique shows higher error than the experimentally obtained curve. One reason for this might be the coherence fluctuations during the experiment.

To concretely assess the error reduction caused by T_1 mitigation technique we need to add error bars to our data. This is underway in the current iteration of the experiment and is part of future research.

6. RESULTS

6.3 Conclusion

We have demonstrated a proof-of-principle Variational Quantum Eigensolver experiment to calculate the ground state energy of H₂. We have designed a novel state preparation ansatz which uses a symmetry of Hydrogen Hamiltonian and is efficient in the number of parameters. We have tested a novel error mitigation technique experimentally. This technique is simple to apply and leads to more than an order of magnitude reduction of error as compared to the VQE experiment without using any error mitigation. The results of the experiment have been consistently compared with simulations using a basic error model. We have compared our results to the quantum chemistry benchmark of chemical accuracy. One the advantages in our approach comes from using the iSWAP gate which can provide a concurrence of 1 in the prepared state in only 8 ns. As a result our experimental sequences are much shorter compared to the state of the art circuit QED experiments which solve the hydrogen problem. However, to use this to advantage we must tune out the buffers in our experimental sequence.

7

Outlook

The first step towards making our simulation of the hydrogen molecule state-of the art should address the high discretization in the angle of iSWAP(θ) gate. This can be done by using the amplitude of the flux pulse as a control knob and not going into resonance (a horizontal cut of chevron pattern of Fig 5.10). The next step should be to implement a numerical optimizer which suggests new parameters and iteratively converges to the ground state energies. The optimization should be implemented for a few points along the dissociation curve as during our initial runs we saw that optimizer takes approximately 500 iterations to converge, corresponding to an overnight of data taking. Moreover, we should tune our readout fidelities better, a higher readout fidelity will enable us to initialize the state by measurement. Our current strategy is to wait for more than $10 T_1$ which is approximately 100. The complete waiting time is governed by fixed point corrections (200) which dictate the time of one shot of experiment. We would need to apply a new fixed point correction if we were to use a new length for the experimental sequence. The above steps would ensure that we fully saturate the potential of Bare VQE.

The T_1 mitigation by post-processing can be implemented in post processing as has been demonstrated. We must refine our results by calculating error bars on the data, to make concrete claims about the error reduction caused by this technique. We should incorporate it in to our optimization process thereby rescaling the expectation values before energy calculation. This way the optimizer already sees cost-fuction which is more accurate, as it is less corrupted by qubit relaxation. We can add another technique called quantum subspace expansion, which has already been demonstrated in circuit QED[ref (16)], to further refine the cost function. We have tested this technique on our datasets with our theory collaborators T.E. O'brien and X.Bonet-Monroig. For a details on the theory of Quantum subspace expansion in the context of Particle conserving circuit, please refer to the Master thesis of X.Bonet-Monroig[ref (3)]. In

7. OUTLOOK

our initial tests we have not seen any improvement in the error by using this technique because of possible error in implementing the technique.

The AEM protocol must be incorporated by repeating the optimization at every chosen bond-length for increasing circuit lengths. Two recent results in circuit qed have shown more than an order of magnitude of error reduction by using variants of this technique on top of Bare VQE[ref (24),(13)]. However, they do not make the claim of reaching chemical accuracy for the entire dissociation curve. By incorporating AEM with the two techniques mentioned above we can aim at reaching the chemical accuracy benchmark.

References

- [1] N. Langford et al. Lecture notes on circuit qed. *arXiv:1310.1897 [quant-ph]*. 37
- [2] Serwan Asaad. Exploring frequency re-use with transmon qubits in a cqed architecture. *Master Thesis, TU Delft*, 2015. 38
- [3] X. Bonet-Monroig. Comparison of error mitigation techniques in a hydrogen molecule quantum simulation. *Master Thesis, Leiden University*, 2018. 67
- [4] J.M. Chow. Quantum information processing with superconducting qubits. *Phd Thesis, Yale University*, 2010. vi, 12, 45, 46
- [5] Michael A. Nielsen Isaac L. Chuang. Quantum computation and quantum information. *Cambridge University Press*. 11
- [6] Livio Cinciaro. Calibration of flux line distortions for two-qubit gates in superconducting qubits. *Master Thesis, TU Delft and ETH Zurich*, 2017. 49, 50
- [7] J. Cramer. Algorithmic speedup and multiplexed readout in scalable circuit qed. *Master Thesis, TU Delft*, 2012. 41, 43, 44
- [8] Abhinav Kandala et. al. Hardware-efficient variational quantum eigensolver for small molecules and quantum magnets. *Nature*, 549, September 2017. 11
- [9] Alberto Peruzzo et. al. A variational eigenvalue solver on a quantum processor. *5213*, 2014 Jul, Jul 2014. 1, 9
- [10] David C. McKay et. al. Efficient z-gates for quantum computing. *arXiv*, 1612.00858v2, 2017. 11
- [11] E Knill et al. Randomized benchmarking of quantum gates. *Physical Review A*, 77(1), 012307, 2008. 37

REFERENCES

- [12] Easwar Magesan et al. Scalable and robust randomized benchmarking of quantum processes. *Phys. Rev. Lett.*, 106(18), 180504, 2011. 37
- [13] E.F. Dumitrescu et. al. Cloud quantum computing of an atomic nucleus. *Phys. Rev. Lett.*, 120, 210501, 2018. 68
- [14] F. Motzoi et al. Simple pulses for elimination of leakage in weakly nonlinear qubits. *Phys. Rev. Lett.*, 103, 110501, 2009. 37
- [15] Ivan Kassal et. al. Simulating chemistry using quantum computers. *Annual Review of Physical Chemistry*, 62:185-207, 2011. 4
- [16] James I. Colless et. al. Robust determination of molecular spectra on a quantum processor. *arXiv*, 1707.06408v1, July 2017. 67
- [17] Jarrod R. McClean et. al. The theory of variational hybrid quantum-classical algorithms. *Annual Review of Physical Chemistry*, 62:185-207, 2011. 3, 16
- [18] Jarrod R. McClean et. al. Openfermion: The electronic structure package for quantum computers. *arXiv*, quant-ph/1710.07629, 2017. 7
- [19] M.A. Rol et al. Restless tuneup of high-fidelity qubit gates. *Phys. Rev. Applied*, 7, 041001, 2017. 39
- [20] Masoud Mohseni et. al. Commercialize quantum technologies in five years. *Nature*, 1710.01022v2, March 2017. 1
- [21] Nikolaj Moll et. al. Quantum optimization using variational algorithms on near-term quantum devices. *arXiv*, 1710.01022v2, Oct 2017. 3, 10
- [22] P.J.J O’Malley et. al. Scalable quantum simulation of molecular energies. *Phys. Rev. X*, 2016. 1, 6, 7, 8, 11
- [23] R.C. Bialczak et. al. Quantum process tomography of a universal entangling gate implemented with josephson phase qubits. *Nature Physics*, 6, 2010. 12, 45
- [24] Abhinav Kandala et.al. Extending the computational reach of a noisy superconducting quantum processor. *arXiv*: 1805.04492v1 [quant-ph], 2018. 68

REFERENCES

- [25] Alexandre Blais et.al. Cavity quantum electrodynamics for superconducting electrical circuits: An architecture for quantum computation. *Physical Review A - Atomic, Molecular, and Optical Physics*, 69(6):062320–1, 2004. 13, 27
- [26] J. M. Chow et.al. Detecting highly entangled states with a joint qubit readout. *Phys. Rev. A*, 81, 062325, 2010. v, 40, 42
- [27] Jens Koch et.al. Charge-insensitive qubit design derived from the cooper pair box. *Physical Review A - Atomic, Molecular, and Optical Physics*, 76(4):1–19, 2007. 25, 29
- [28] Kristan Temme et.al. Error mitigation for short-depth quantum circuits. *Physical Review A - Atomic, Molecular, and Optical Physics*, arXiv, November 2017. 17, 19
- [29] L. DiCarlo et.al. Demonstration of two-qubit algorithms with a superconducting quantumprocessor. *Nature*, 460(7252):240–244, 2009. 45
- [30] X.Fu et.al. An experimental microarchitecture for a superconducting quantum processor, 2017. 35, 36
- [31] Peter J. Love Jacob T. Seeley, Martin J. Richard. The bravyi-kitaev transformation for quantum computation of electronic structure. *The Journal of Chemical Physics*, 137, 224109, 2012. 5, 6
- [32] Alán Aspuru-Guzik James D. Whitfield, Jacob Biamonte. Simulation of electronic structure hamiltonians using quantum computers. *arXiv:1001.3855*, 2010. 4
- [33] Y. Li. Private Communication, 2017. 17
- [34] Ying Li and Simon C. Benjamin. Efficient variational quantum simulator incorporating active error minimization. *Phys. Rev. X*, 7, 021050, June 2017. 17
- [35] Brian Tarasinski-Ramiro Sagastizabal Cornelis Christiaan Bultink Malay Singh Leonardo DiCarlo Michiel Adriaan Rol, Livio Ciociaro. A qubit-based oscilloscope for characterizing the distortion of flux pulses for two-qubit gates in circuit qed. *Bulletin of the American Physical Society*, to be published. 49
- [36] Michael A. Nielsen. The fermionic canonical commutation relations and the jordan-wigner transform. *Blog of Michael Nielsen*. 6
- [37] T.E. O'Brien. Private Communication, 2017. 22

REFERENCES

- [38] TE O'Brien et.al. Density-matrix simulation of small surface codes under current and projected experimental noise. *npj Quantum Information* 3, 39, September 2017. 1, 13, 23
- [39] Peter James Joyce O'Malley. Superconducting qubits: Dephasing and quantum chemistry. 6
- [40] John Pople. Nobel lecture: Quantum chemical models. *Rev. Mod. Phys.*, 71, 1267, 1999. 3
- [41] Matthew David Reed. Entanglement and quantum error correction with superconducting qubits. *PhD Thesis, Yale University*, 2013. 37
- [42] Alexei Kitaev Sergey Bravyi. Fermionic quantum computation. *arXiv*, quant-ph/0003137, 2000. 6
- [43] Christian Dickel et.al Serwan Asaad. Independent, extensible control of same-frequency superconducting qubits by selective broadcasting. *npj Quantum Information*, 2:16029, 2016. 39
- [44] Daniel G. A. Smith. Psi4numpy: An interactive quantum chemistry programming environment for reference implementations and rapid development. *J. Chem. Theory Comput.*, 10.1021, 2018. 7
- [45] P.Jorgensen T.Helgaker and J.Olsen. Molecular electronic structure theory. *Wiley, New York*, 2002. 3